

THE INFRARED MEDIUM-DEEP SURVEY. II. HOW TO TRIGGER RADIO AGNs? HINTS FROM THEIR ENVIRONMENTS

MARIOS KAROUZOS¹, MYUNGSHIN IM¹, JAE-WOO KIM¹, SEONG-KOOK LEE¹, SCOTT CHAPMAN², YISEUL JEON¹, CHANGSU CHOI¹,
JUEUN HONG¹, MINHEE HYUN¹, HYUNSUNG DAVID JUN¹, DOHYEONG KIM¹, YONGJUNG KIM¹, JI HOON KIM^{1,3}, DUHO KIM^{1,4},
SOOJONG PAK⁵, WON-KEE PARK^{1,6}, YOON CHAN TAAK¹, YONGMIN YOON¹, AND ALASTAIR EDGE⁷

¹ CEOU—Astronomy Program, Department of Physics & Astronomy, Seoul National University, Gwanak-gu, Seoul 151-742, Korea

² Department of Physics and Atmospheric Science, Dalhousie University, Halifax, Nova Scotia, Canada; mkarouzos@astro.snu.ac.kr

³ Subaru Telescope, National Astronomical Observatory of Japan, 650 North A'ohoku Place, Hilo, HI 96720, USA

⁴ Arizona State University, School of Earth and Space Exploration, P.O. Box 871404, Tempe, AZ 85287-1404, USA

⁵ School of Space Research, Kyung Hee University, Yongin-si, Gyeonggi-do 446-701, Korea

⁶ Korea Astronomy and Space Science Institute, 776 Daedeokdae-ro, Yuseong-gu, Daejeon 305-348, Korea

⁷ Department of Physics, University of Durham, South Road, Durham, DH1 3LE, UK

Received 2014 July 7; accepted 2014 October 10; published 2014 November 21

ABSTRACT

Activity at the centers of galaxies, during which the central supermassive black hole is accreting material, is nowadays accepted to be rather ubiquitous and most probably a phase of every galaxy's evolution. It has been suggested that galactic mergers and interactions may be the culprits behind the triggering of nuclear activity. We use near-infrared data from the new Infrared Medium-Deep Survey and the Deep eXtragalactic Survey of the VIMOS-SA22 field and radio data at 1.4 GHz from the FIRST survey and a deep Very Large Array survey to study the environments of radio active galactic nuclei (AGNs) over an area of $\sim 25 \text{ deg}^2$ and down to a radio flux limit of 0.1 mJy and a *J*-band magnitude of 23 mag AB. Radio AGNs are predominantly found in environments similar to those of control galaxies at similar redshift, *J*-band magnitude, and $(M_u - M_r)$ rest-frame color. However, a subpopulation of radio AGNs is found in environments up to 100 times denser than their control sources. We thus preclude merging as the dominant triggering mechanism of radio AGNs. By fitting the broadband spectral energy distribution of radio AGNs in the least and most dense environments, we find that those in the least dense environments show higher radio-loudness, higher star formation efficiencies, and higher accretion rates, typical of the so-called high-excitation radio AGNs. These differences tend to disappear at $z > 1$. We interpret our results in terms of a different triggering mechanism for these sources that is driven by mass loss through winds of young stars created during the observed ongoing star formation.

Key words: galaxies: active – galaxies: jets – galaxies: star formation – galaxies: statistics – Galaxy: evolution – infrared: galaxies – radio continuum: galaxies

Online-only material: color figures

1. INTRODUCTION

There is an ongoing debate as to what the possible triggers of activity in the nuclei of galaxies may be. In a fundamental sense, the triggering of active galactic nuclei (AGNs) requires the availability of a gas reservoir that feeds the accretion onto the supermassive black hole at the center of a galaxy. Traditionally, the high incidence of merger remnants within samples of powerful quasars (e.g., Heckman et al. 1986; Canalizo et al. 2007; Bennert et al. 2008; Karouzos et al. 2010; Ramos Almeida et al. 2011), the temporal coincidence of cosmic AGNs and star formation activity (e.g., Hopkins & Beacom 2006; Richards et al. 2006; Aird et al. 2010; Kistler et al. 2013), and the phenomenological link between a local population of ultraluminous infrared galaxies and powerful obscured quasars (e.g., Sanders et al. 1988; Canalizo & Stockton 2001) has led to the first-order conclusion that AGNs might be triggered through the merging of gas-rich galaxies (e.g., Hernquist 1989; Kauffmann & Haehnelt 2000; Lotz et al. 2008). The gas available during such violent processes should trigger both bursts of intense star formation and consequently a phase of efficient accretion onto the central supermassive black hole (e.g., Hopkins et al. 2006), potentially with a time lag between the two phases (e.g., Wild et al. 2010).

While this scenario has been successful in explaining how powerful AGNs are triggered during galactic mergers (although

even this is still heavily debated; e.g., Villforth et al. 2014; Karouzos et al. 2014b), it soon became evident that such mergers of gas-rich galaxies cannot explain the full population of active galaxies. Especially in the local and intermediate-redshift universe, the rate of these major mergers decreases significantly (e.g., Lotz et al. 2011). Several studies of the morphologies of moderate-luminosity X-ray AGNs (i.e., efficient accretors) at low and intermediate redshifts have shown that the morphologies of their host galaxies lack evidence of recent or ongoing mergers (e.g., Cisternas et al. 2011; Kocevski 2012) but rather show prominent disks. The morphological end product of a potential major merger would be a “red and dead” early-type galaxy (e.g., Hopkins et al. 2008). Moreover, a different flavor of active galaxies, AGNs exhibiting strong collimated outflows in the radio (radio AGNs; e.g., Urry & Padovani 1995), were understood to be predominantly inefficiently accreting systems (e.g., Kauffmann et al. 2003a; Best et al. 2005a; Hardcastle et al. 2007), which could be very easily fed with a moderate amount of gas, either cold or hot, potentially originating in the halo of their host galaxy (e.g., Hopkins & Hernquist 2006). As such, there should be a significant population of active galaxies that is unassociated with mergers, their triggering and evolution rather driven by secular processes.

Previous studies on this topic focusing on the morphologies of AGN host galaxies have been plagued by two major

drawbacks. Given the potential time lag between the peak of AGN luminosity and the peak of a galactic merger (e.g., Sanders et al. 1988), AGN-selected samples should exhibit very faint merger features and tidal distortions (e.g., Lotz et al. 2008), if any. The detection of these faint morphological features requires long exposure times and ideal observing conditions. The situation is aggravated by the fact that luminous AGNs significantly contaminate, or in some cases even completely overshadow, the light of their host galaxy (e.g., Pierce et al. 2010). Therefore, very high dynamic range, high-resolution imaging is required to disentangle the different emission components. As a result, the number of AGN host galaxies that can be properly observed is constrained in terms of both AGN luminosity and host galaxy stellar mass.

An alternative approach to answer the question of what triggers AGNs, over a range of AGN luminosities and independent of host galaxy luminosity, is the study of their environments. The density of the environment within which an AGN is embedded can be used as a proxy not only of past but also of near-future mergers. It is expected that if mergers play a significant role in the triggering of AGNs, they should be found in denser small-scale⁸ environments than other galaxies of similar properties. As in the case of morphology studies, the inferences from the study of AGN environment have largely been dependent on the wavelength in which the AGNs were selected. Results range from AGNs found in significantly overdense (OD) environments (e.g., Best 2004; Serber et al. 2006; Tasse et al. 2008; Ellison et al. 2011; Bradshaw et al. 2011; Satyapal et al. 2014; Pace & Salim 2014) to environments that are consistent or even underdense (UD) compared to those of nonactive galaxies with similar galaxy properties (e.g., Miller et al. 2003; Kauffmann et al. 2004; Tasse et al. 2011). In particular, Karouzos et al. (2014b), using the first data release of the VIDEO survey (Jarvis et al. 2013), showed that the bulk of AGNs, irrespective of the wavelength selection, reside in rather unremarkable environments when compared to nonactive galaxies of similar stellar mass, out to a redshift of $z = 3$. In the same study, it was shown that among the differently selected AGNs, radio AGNs showed the highest degrees of overdensities among radio-, X-ray-, and mid-IR-selected active galaxies. Moreover, radio AGNs were found to preferentially inhabit denser environments at group scales (<200 kpc) rather than cluster scales (~ 1 Mpc).

Here we expand on our previous study (Karouzos et al. 2014b), by focusing on a radio-selected sample of AGNs, covering a much larger part of the sky than the first data release VIDEO sample (~ 1 deg²), refining our control sample selection, and expanding the radio luminosity range probed to eight orders of magnitude. As such, we are in a position to counter the possible cosmic variance effects affecting small-area survey fields. Furthermore, by including the relatively rare very radio-luminous AGNs, we test the possible dichotomy of triggering mechanisms between faint and luminous AGNs. Finally, we take the study of the environments of radio AGNs a step further by looking at the host galaxy properties of these sources and making a connection between the small-scale environments of AGNs and the potential feeding mechanisms of their supermassive black holes.

The paper is organized as follows. In Section 2, we describe the data we use in this paper, in particular introducing the Infrared Medium-Deep Survey (IMS). In Section 3, the method-

ology of this study is described, explaining the calculation of photometric redshifts, the selection of control samples, and the fitting of the broadband spectral energy distribution (SED) undertaken. In Section 4, we present our results concerning the environments of radio AGNs, while in Section 5, we make the connection between the environments of radio AGNs and their host galaxy properties. Finally, in Sections 6 and 7, we discuss the implications of our results in the context of other studies in the literature and offer our final conclusions, respectively. Throughout the paper, we assume the cosmological parameters $H_0 = 71$ km s⁻¹ Mpc⁻¹, $\Omega_M = 0.27$, and $\Omega_\Lambda = 0.73$ (Komatsu et al. 2011).

2. THE SA22 FIELD

2.1. Near-infrared Surveys in the SA22 Field

IMS (M. Im et al., in preparation) is a recently concluded near-infrared (NIR) imaging survey using the United Kingdom Infrared Telescope (UKIRT) Wide Field Camera (WFCAM; Casali et al. 2007) on the 3.8 m UKIRT in Hawaii, the Seoul National University CAMera (SNUCAM; Im et al. 2010) on the 1.5 m telescope at the Maidanak Observatory in Uzbekistan, and the Camera for QUasars in the EARly uNiverse (CQUEAN; Park et al. 2012) on the 2.1 m Otto-Struve Telescope at the McDonald Observatory in Texas. The IMS covers ~ 106 deg² on the sky in Y and J NIR bands, with a 5σ magnitude limit of 23 mag AB. Through the IMS some of the most well-known extragalactic legacy survey fields have been observed in the NIR. These include the *XMM* Large Scale Structure, the Canada-France-Hawaii Telescope (CFHT) Legacy Survey W2, the Lockman Hole, the Extended Groth Strip, the European Large Area Infrared Survey North 1 and 2, and the SA22 fields.

In particular, here we focus on the SA22 field as a result of its good wavelength coverage in both the NIR from the IMS (J band, covering a total of 16 deg²) and the optical by the CFHT Legacy Survey (CFHTLS; u , g , r , i , and z). In addition, part of the SA22 field is covered by the Deep eXtragalactic Survey (DXS), part of the UKIRT Infrared Deep Sky Survey (UKIDSS; Lawrence et al. 2007), which provides additional K_s -band coverage down to a magnitude limit of 22.7 mag AB (5σ limit; Kim et al. 2011) for a total of 8.75 deg². A coverage map of the SA22 field is shown in Figure 1.

As we are interested in measuring the environment properties of galaxies, the accurate knowledge of distances and hence redshifts is imperative. Given the absence of full spectroscopic coverage of the SA22 field, it is crucial to acquire accurate galaxy colors for the calculation of robust photometric redshifts. Therefore, for our analysis we use a point-spread function (PSF) matched band-merged catalog.⁹ In short, we use a Gaussian PSF of $1''.1$ (equal to the worst seeing among all SA22 observations) to convolve images at all bands. The convolved images are then resampled to match the WFCAM field of view and CFHT pixel scale (0.8 deg² and $0''.187$ pixel⁻¹) using the SWARP package (Bertin et al. 2002). The original (prior to PSF matching) J -band image is then used as the detection image. After that we use the SExtractor software (Bertin & Arnouts 1996) in dual mode to extract sources from the images in the rest of the photometric bands.¹⁰ The multiwavelength data available in the SA22 field and their respective limits are shown in Table 1. Our

⁸ Here “small scale” is defined as <500 and is associated with close companions and galaxy group environments. Conversely, “large scale” relates to galaxy cluster environments at linear scales of ~ 1 Mpc.

⁹ The detailed catalog construction and full catalog will be presented in J. W. Kim et al. (2014, in preparation).

¹⁰ An aperture of 2 is used for aperture magnitude extraction in SExtractor.

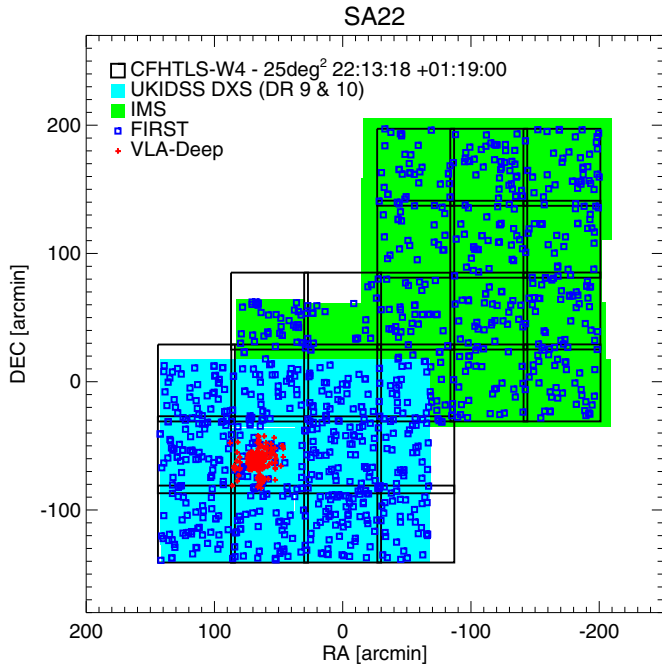


Figure 1. Coverage map of the SA22 field showing the coverage of the IMS and DXS NIR surveys and the CFHT optical survey. The cross-matched radio sources (see Section 2.3) from the VLA-FIRST (blue squares) and VLA-Deep (red circles) radio surveys are also shown. The map is centered at the center of the CFHTLS W4 field (22:13:18, +01:19:00).

(A color version of this figure is available in the online journal.)

base selection is done in the J band at IMS’s limiting magnitude (23 mag AB) over the total area of ~ 25 deg².

2.2. Radio Surveys in the SA22 Field

For the selection of radio sources we use data from the Faint Images of the Radio Sky at Twenty cm (FIRST; Becker et al. 1995), a very wide field radio survey at 1.4 GHz using the Very Large Array (VLA) radio interferometer. The FIRST survey has a flux density limit of 1 mJy and a resolution of 5". We exclude radio sources from the FIRST survey catalog that have a probability, $P(S)$, to be spurious owing to sidelobes of neighboring bright sources $P(S) > 0.15$ (for the way $P(S)$ is defined and calculated, see White et al. 1997). In addition, we use a deeper radio survey of part of the SA22 field using the VLA at two different configurations, A (PI: Chapman) and B (PI: Yun), with a limiting flux density of ~ 0.05 – 0.12 mJy beam⁻¹ (5σ limit) and a resolution of 1".4 and 5", respectively. More details on these data are given in Appendix A.

2.3. Radio–IR Source Cross-matching

In order to study the environments and host galaxy properties of radio sources in the SA22 field, we cross-match our base J -band catalog with the two radio catalogs for the SA22 field. We use the Poisson-probability-based method of Downes et al. (1986) (e.g., Ivison et al. 2007; Hodge et al. 2013). The proximity and magnitude of each individual candidate source are used to calculate the probability that the candidate source is not a background source, P . Around each radio source we calculate the Poisson probability for each NIR source to be within a circle of radius r_c . This Poisson probability is defined as

$$P^* = 1 - e^{-\pi r_c^2 N_m},$$

Table 1

Information about the Photometric Data Available for the SA22 Field and in Particular for the IR–radio Cross-matched Sample (VLA-FIRST Sample)

Survey	Band	Wavelength (μm)	Sensitivity (AB mag)
CFHTLS	u^*	0.38	25.2
	g	0.48	25.5
	r	0.62	25.0
	i	0.75	24.8
	z	0.88	23.9
IMS	J	1.2	23.0
UKIDSS DXS	J	1.2	23.2
	K_s	2.2	22.7
WISE-All Sky Survey	$W1$	3.4	20.0
	$W2$	4.6	19.3
	$W3$	12.0	17.0
	$W4$	22.0	14.7
VLA-FIRST	L	1.4 ^a	1.0 ^b
VLA-Deep	L	1.4 ^a	0.1 ^b

Notes. Column 1 gives the name of the survey, and Columns 2, 3, and 4 give the waveband name, central wavelength, and sensitivity (5σ), respectively.

^a Frequency in units of GHz.

^b Units for the VLA band are given in units of mJy.

where r is the distance of the candidate counterpart from the multiwavelength source, and N_m is the surface number density within radius r and limiting NIR magnitude m . Parameter r_c can be defined through the angular resolution of the different instruments (i.e., WFCAM and VLA). Here we assume an $r_c = 10''$, which is two times the nominal resolution of the FIRST survey.¹¹ The expected number of events (i.e., NIR sources) with $P \leq P^*$ can then be approximated (for a finite search radius r_c) as

$$E = P_c = \pi r_c^2 N_T,$$

for $P^* \geq P_c$, and

$$E = P^*(1 + \ln P_c/P^*),$$

for $P^* < P_c$. P_c is a critical Poisson probability, defined by the surface number density, N_T , at the limiting magnitude of the NIR sample.

Finally, the probability of a chance cross-identification of the source can be calculated as $1 - e^{-E}$. The NIR candidate with the lowest such probability is chosen to be the true counterpart. For the FIRST sample, 1482 sources are matched to an NIR source. Of these, 67 radio sources are matched with 33 NIR sources in double or triple matches (32 cases and one case where the same NIR source was matched with two and three FIRST radio sources, respectively). For the VLA-Deep sample, in total 204 sources are matched to an NIR source. Of these, 16 are part of double cross-matchings with the same NIR source.

The occurrence of a double cross-matching of two radio sources with a single NIR source may imply the presence of a double-lobe radio source (Fanaroff–Riley class II object, FR II; Fanaroff & Riley 1974) or a core-jet configuration radio source. We combine the calculated Poisson probabilities and source separation with the classification scheme described in Best et al. (2005a) to decide whether a multiple association is a true or a spurious one.

¹¹ In practice, the majority of NIR sources ($\sim 70\%$) are at distances found below 5" from their matched radio source.

1. For cases where one radio source is found very close to the NIR source ($r < 5''$) and has very low probability for chance cross-matching ($< 10\%$), while the other(s) is at $r > 5''$ and with high probability for chance cross-matching, the latter is considered spurious and the first one is kept.
2. For cross-matchings where all radio sources have $r > 5''$ and probability for chance cross-matching $> 10\%$, all of them are considered spurious and removed from the sample.
3. For the rest of the cases, the multiple matching is flagged as a candidate for a multicomponent radio source. For these cases we follow the scheme of Best et al. (2005a). In short, if one of the radio sources is at $r < 3''$ from the NIR source while the others are not, this is considered a core-jet candidate, and a comparison with the NRAO VLA Sky Survey (NVSS; Condon et al. 1998) is required. Among our sources we do not have such a case. Alternatively, if the flux-weighted position of the two radio sources is close to the NIR one (here we assume a limit of $1''.5$) and the two radio sources have comparable radio flux densities (here < 1 mJy), then this is classified as a double-lobe radio source.

For the FIRST sample, seven multiple matchings fall within case 1 (one matching considered as true), eight multiple matchings fall within case 3 (double-lobe radio sources), while the rest fall under case 2 and are discarded as spurious. For the VLA-Deep sample, five multiple matchings fall under case 1, with the rest being discarded as spurious as no multiple matchings fulfill the criteria of a double-lobe radio source. Given the small number of actual double-lobe radio sources in our sample and in the absence of multifrequency information that would confirm or reject this classification, we decide to exclude these eight double-lobe radio source candidates from any further analysis. In the end, the FIRST-NIR cross-matched sample contains 1424 sources, and the VLA-Deep-NIR sample contains 193 sources (the positions of these sources within the SA22 field are shown in Figure 1). The radio flux densities and J -band magnitudes of the final radio sample are shown in Figure 2.

In order to select radio AGNs in these two samples, we employ a radio luminosity limit cut at 1.4 GHz. Following Condon (1992), we can define a limiting nonthermal radio luminosity above which a source can be classified as an AGN:

$$\left(\frac{L_N}{W \cdot \text{Hz}^{-1}} \right) \sim 5.3 \times 10^{21} \left(\frac{\nu}{\text{GHz}} \right)^{-\alpha} \left[\frac{\text{SFR} (M \geq 5M_\odot)}{M_\odot \text{ yr}^{-1}} \right], \quad (1)$$

where L_N is the nonthermal luminosity produced from ongoing star formation with a star formation rate (SFR) at an observing frequency ν and with a radio spectral index $\alpha = 0.8$. We set a threshold of 100 solar masses per year, which gives a critical luminosity of $L_{\text{lim}} = 1.03 \times 10^{40} \text{ erg s}^{-1}$. This roughly matches the turnover power of the local luminosity function of radio sources, above which radio-loud AGNs dominate the radio-source population (e.g., Best et al. 2005b; Mauch & Sadler 2007). After K -correcting the 1.4 GHz luminosities of the VLA sources (see Section 3.1 for information on how redshifts were derived), objects more luminous than the above limit are assumed to be AGNs. Given the absence of multifrequency radio data, we make the assumption of an average radio spectral index of $\alpha = 0.8$ (e.g., Condon 1992). There are 777 FIRST sources and 136 VLA-Deep sources classified as radio AGNs according to this criterion. Table 2 gives the names and sizes of the different (sub)samples used in the rest of the paper, along

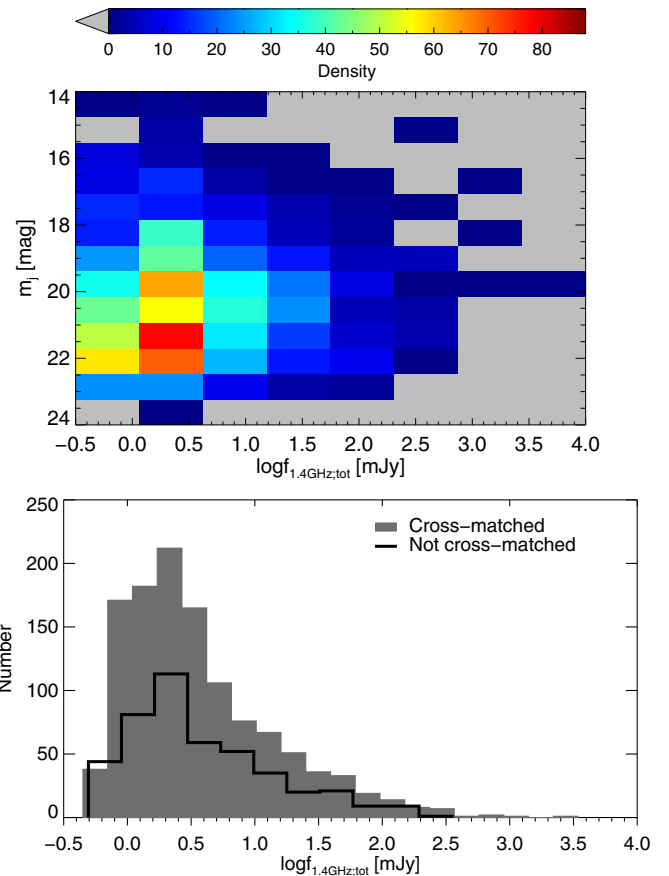


Figure 2. Distribution of radio flux densities and J -band magnitudes for the cross-matched and non-cross-matched radio samples in the SA22 field. Upper: density map of the J -band magnitude vs. flux density at 1.4 GHz (in logarithmic scale). Lower: flux density distribution at 1.4 GHz for cross-matched (shaded histogram) and nonmatched (open histogram) radio samples.

(A color version of this figure is available in the online journal.)

with the relevant sections where they are first introduced, and a description of their selection criteria.

3. METHODOLOGY AND ANALYSIS

3.1. Photometric Redshifts

For the study of the environment, information about the distances between sources and from the sources to the observer are needed. The SA22 field has been partly observed by the VIRMOS-VLT Deep Spectroscopic Survey (VVDS; Le Fèvre et al. 2005), down to an i -band AB magnitude of 22.5. In total, there are 6751 spectroscopic redshifts within the SA22 field (we use a cross-matching radius of $1''$ to associate spectroscopic sources with NIR sources). In addition to these, we use the publicly available photometric redshift code LePhare (Arnouts et al. 1999; Ilbert et al. 2006) to calculate photometric redshifts for the rest of the SA22 sources using a total of seven broadband photometric bands for the full SA22 field and additionally K_s band for the part covered by DXS.

For the photometric redshift calculation we use the set of CFHT galaxy SED templates from Ilbert et al. (2006) and the Polletta et al. (2007) and Salvato et al. (2011) AGN templates (these also include composite AGN and star-forming systems). In addition, we use stellar template libraries to identify and exclude stars from our sample. We use 3609 reliable spectroscopic redshifts from VVDS to calibrate our photometric redshift calculation, by deriving the possible photometric band

Table 2
Radio (Sub)Samples Overview

(Sub-)Sample	Section	Number	Description
FIRST; All	3, 4	1009	FIRST/IMS cross-match
FIRST; AGN	3, 4	777	FIRST/IMS, $L_{1.4\text{GHz}} \gtrsim 10^{40} \text{ erg s}^{-1}$
VLA-Deep; All	3, 4	181	VLA-Deep/IMS cross-match
VLA-Deep; AGN	3, 4	136	VLA-Deep/IMS, $L_{1.4\text{GHz}} \gtrsim 10^{40} \text{ erg s}^{-1}$
DXS; Radio AGNs	5	689	Radio/IMS, $L_{1.4\text{GHz}} \gtrsim 10^{40} \text{ erg s}^{-1}$, DXS area
DXS; Over-Dense	5	77 (49)	Radio/IMS, $L_{1.4\text{GHz}} \gtrsim 10^{40} \text{ erg s}^{-1}$, DXS area, overdense environments
DXS; Under-Dense	5	31 (24)	Radio/IMS, $L_{1.4\text{GHz}} \gtrsim 10^{40} \text{ erg s}^{-1}$, DXS area, underdense environments

Notes. Summary of the (sub)samples used throughout the paper (Column 1), along with the section where they are first introduced (Column 2) and their size (Column 3). For the last two rows, in brackets we give the number of sources identified as with reliable SEDs (see Section 5 and Figure 14). A summary of the definitions and selection criteria of each sample is shown in the last column, but more details can be found in the respective sections.

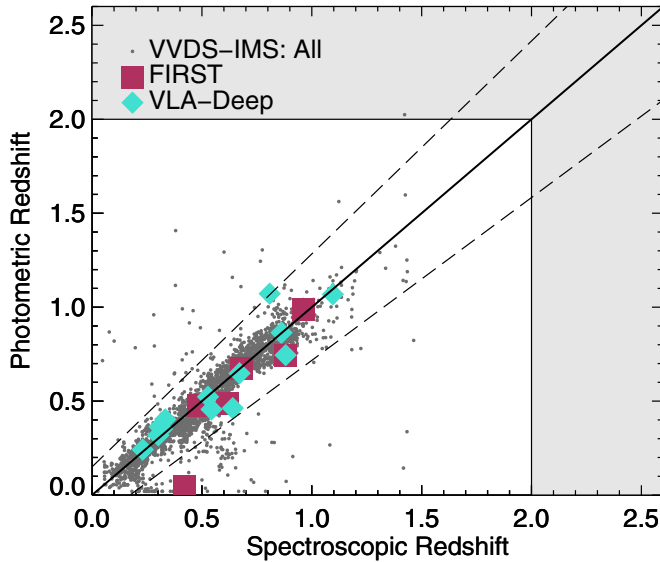


Figure 3. Comparison between the spectroscopic redshifts from VVDS and photometric redshifts within the SA22 field. Gray dots show all sources with good-quality spectroscopic redshifts (Flags 3 and 4). Large symbols show radio sources from the FIRST and VLA-Deep samples with spectroscopic redshifts (maroon squares and turquoise diamonds, respectively). We show our sample selection at $z < 2$ with the vertical and horizontal lines. The diagonal solid line shows the one-to-one relationship, and the dashed lines represent a 15% deviation from the solid line.

(A color version of this figure is available in the online journal.)

offsets that have been shown to exist (e.g., Ilbert et al. 2006). The comparison between the spectroscopic and photometric redshifts is shown in Figure 3.

Using the iterative method of Ilbert et al. (2006) implemented in the LePhare code, we calculate the photometric band offsets. We find these to be mostly below 0.1 mag (only one band, J , exhibits an offset of 0.24), with a mean value of 0.06 mag. From the comparison between the spectroscopic and photometric redshifts, we get a normalized median absolute deviation (Ilbert et al. 2006) of $\sigma_{\text{NMAD}} = 0.038$ and an outlier fraction of 4.8%.¹²

In Figure 3, we also show the comparison for the radio sources in the FIRST and VLA-Deep samples with available spectroscopic redshifts. Although we note the small number from which a conclusion can be drawn, all but two of the radio sources show good agreement between their spectroscopic and photometric redshifts, when considering the best-fit photometric

¹² Here we follow the standard definition of outliers as $\delta z / (1+z) > 0.15$.

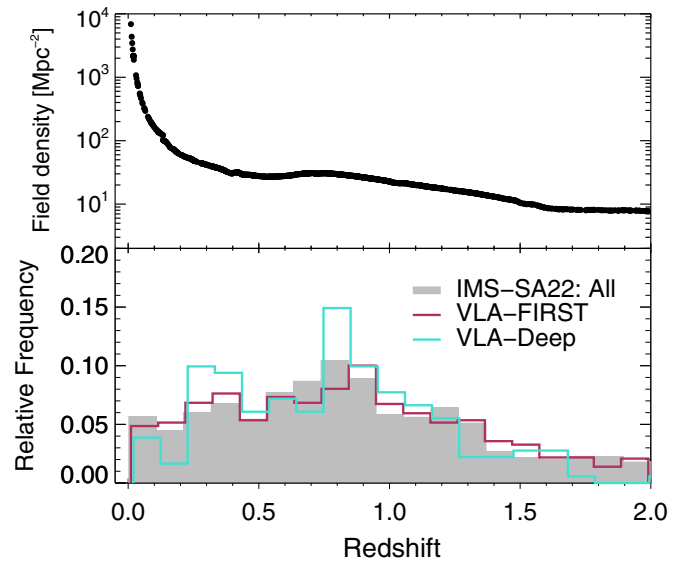


Figure 4. Upper: source number density per unit square area within finite redshift slices of depth $0.2(1+z)$ as a function of redshift, for the total sample. Lower: redshift distribution for the total SA22 sample (gray-shaded histogram), the VLA-FIRST sample (maroon open histogram), and the VLA-Deep sample (turquoise open histogram).

(A color version of this figure is available in the online journal.)

redshift from galaxy templates only. This translates nevertheless to an outlier fraction that is double that of the base sample ($\sim 10\%$).¹³ On the other hand, if we consider both galaxy and AGN templates for the determination of the best photometric redshift (in terms of the χ^2 result of the fit), the number of outliers increases dramatically, resulting in an outlier fraction of $\sim 44\%$. Given the relatively small number of radio sources with spectroscopic redshifts, it is impossible to calibrate our AGN template photometric redshift determination any further. As such, we decide to consider photometric redshifts derived only from galaxy template fits. This is a reasonable approximation for both star-forming galaxies, found at low radio luminosities, and the majority of radio AGNs, whose optical and NIR SEDs are usually not dominated by an AGN component.

In Figure 4, we show the redshift distribution for the total SA22 field and those of the two radio samples. In addition, in

¹³ The two outliers do not appear to stand out in some consistent way in their radio or optical properties from the rest of the radio sample. They both exhibit intermediate optical luminosities ($\sim 10^{43} \text{ erg s}^{-1}$), and while one appears to be very luminous at 1.4 GHz ($\sim 10^{43} \text{ erg s}^{-1}$), the other one is right on the AGN radio-luminosity limit ($\sim 10^{40} \text{ erg s}^{-1}$).

Figure 4, the source pseudo-3D density is shown as a function of redshift. The density is calculated within finite slices of redshift with a width of $0.2(1+z)$ and is defined as the total number of sources within a given redshift slice divided by the total area covered by the SA22 survey at that redshift. We see that the field density falls smoothly as a function of redshift, owing to the flux-limited nature of our sample. Concerning the redshift distribution of the two radio samples, they do not exhibit obvious differences. The VLA-FIRST sample appears to extend to slightly higher redshifts than the VLA-Deep one.

Finally, LePhare also provides the estimated absolute magnitudes in the observed filters ($ugrizYJK_s$). In particular, we use the method detailed in Ilbert et al. (2005), which should be less template dependent than other alternatives offered in the LePhare code. As will be explained in Section 3.3, we shall use the $(M_u - M_r)$ rest-frame absolute magnitude color to select a control sample for the radio sources. In Figure 5, we compare the distributions of $(M_u - M_r)$ rest-frame absolute magnitude color between the FIRST and VLA-Deep samples. As can be seen in Figure 5, the VLA-Deep sources show on average bluer colors. This is expected as deep, small-area surveys with a significant sub-mJy source component tend to be dominated by star-forming galaxies and star-forming/AGN composite systems (e.g., Seymour et al. 2008; Padovani et al. 2009).

3.2. Environment Density Parameters

We employ the distance to the n th closest neighbor to define the surface density parameter Σ_n , originally introduced by Dressler (1980). This is defined as

$$\Sigma_n = \frac{n}{\pi d_n^2}.$$

To identify the closest neighbor and calculate its distance to a radio source, we look within a redshift slice of $\pm 0.1(1+z)$. In this way we can calculate a pseudo-3D density. As we are interested in the close environments of radio AGNs, to look for signs of mergers, we concentrate our analysis on the second- and fifth-closest neighbors.¹⁴ Given the finite resolution of our observations and the large difference between the resolution in the NIR and the radio ($\sim 1''$ compared to $\sim 5''$, respectively) we do not use the distance to the closest neighbor. Following Cooper et al. (2005), to minimize the contamination from edge effects, we exclude sources at a distance of $2'$ from the field edges. For the calculation of both density parameters and projected distance to the n th-closest neighbor, we consider the total, band-merged, SA22 sample, excluding only sources with stellar-like colors (as identified from the photometric redshift fitting process).

We define the measure of overdensity for our study as the ratio between the density parameter of a radio source (i.e., Σ_i^{radio} , where $i = \{2, 5\}$) and the mean density parameter of its random and matched control sample (i.e., $\bar{\Sigma}_i^{\text{cont}}$, where $i = \{2, 5\}$). As such, for $\Sigma_i^{\text{radio}} > \bar{\Sigma}_i^{\text{cont}}$ it follows that the overdensity ratio takes values above 1. Similarly, for $\Sigma_i^{\text{radio}} < \bar{\Sigma}_i^{\text{cont}}$ the overdensity ratio has a value below 1. The definition of the overdensity measure in terms of the density ratio between a radio source and its control sources alleviates problems related to the flux-limited nature of our samples. Specifically, it addresses the fact that at higher redshifts the selected sample tends to be increasingly dominated by more luminous and hence potentially more massive galaxies.

¹⁴ For our sample, mean projected distance to the second-closest neighbor is $D_2 = 127$ kpc, and for the fifth-closest neighbor it is $D_5 = 217$ kpc. These linear scales are well below typical cluster scales and are therefore more relevant to close companions or group environments.

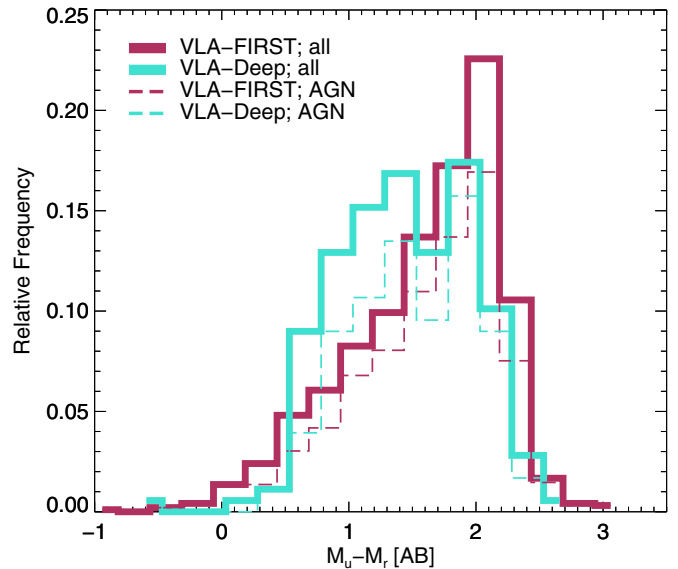


Figure 5. Rest-frame absolute magnitude color ($M_u - M_r$) relative distributions for the FIRST (maroon histograms) and VLA-Deep (turquoise histograms) radio samples. We differentiate between the total samples (solid thick lines) and the AGN subsamples defined through their 1.4 GHz radio luminosity (dashed thin lines).

(A color version of this figure is available in the online journal.)

3.3. Control Samples

The robust selection of a control sample is fundamental in being able to draw robust conclusions concerning the environment of radio AGNs. The criteria for our matched control sample selection are driven by the needs of our study and the properties of our base sample. Therefore, we essentially impose a matching of J -band luminosity (the reddest band available for the entirety of the SA22 field), as it is, among the available photometry, the band least affected by obscuration. As we are dealing with radio AGNs, we do not need to worry about a significant contamination in the optical and NIR parts of the SED from the AGNs, as the optical and NIR properties of radio AGNs have been found to be largely independent of their radio properties (e.g., Best et al. 2005a). In a similar manner, we match the $(M_u - M_r)$ rest-frame absolute color, as this is a good measure of star formation in galaxies (essentially covering the 4000 Å break; e.g., Kauffmann et al. 2003b), as well as their morphologies (e.g., Strateva et al. 2001). Furthermore, it has been shown that the clustering of galaxies appears to be strongly dependent on their color (e.g., Skibba et al. 2014; Zehavi et al. 2011; Coil et al. 2008), with the general consensus being that redder and hence lower star formation galaxies are more strongly clustered than their bluer counterparts.

As such, we select two control samples, one that should reflect the average field density at a given redshift (random control sample) and one that aims to match each AGN with a group of control sources of similar redshift, magnitude, and rest-frame color (matched control sample). In more detail, for the random control sample, for each radio source we select 20–40 random positions within the SA22 field, not necessarily associated with a source. We then compute the environment properties around each of these positions assuming the redshift of the radio source. The average of these is assigned as the random control value of this radio source. Similarly, for the matched control sample, for each radio source we select 20–40 control sources with the SA22 field that fulfill the following criteria:

1. $|z_{\text{radio}} - z_{\text{control}}| \leq 0.1(1 + z_{\text{radio}})$;
2. $|J_{\text{radio;obs}} - J_{\text{control;obs}}| \leq 0.2$; and
3. $|(M_u - M_r)_{\text{radio;rest}} - (M_u - M_r)_{\text{control;rest}}| \leq 0.2$.

We then again calculate the average environment properties for these control sources and assign this value as the matched control value to the radio source. For both samples, we pay special attention to edge effects (e.g., Cooper et al. 2005) and also avoid selecting random and matched control sources around bright stars and otherwise masked problematic areas of the images. Finally, we also ensure that each of the random positions and matched control sources are not within $60''$ of their respective radio source in order to minimize any contamination from local over- or underdensities around the radio source.

3.4. Broadband Spectral Energy Distributions

An important component of this study is the link between the host galaxy properties of radio AGNs and their environments. To that end, we undertake the model fitting of the broadband SEDs of the radio sources in our sample. For that we use the full wavelength coverage ranging the optical and the NIR. Given the importance of K_s band to constrain the old stellar population component and hence the star formation history (SFH) of a galaxy, we constrain the SED fitting to galaxies covered by the DXS and thus observed in the K_s band. This reduces the available sources to a total of 711 radio sources (530 in the FIRST and all 181 sources from the VLA-Deep survey). Nevertheless, at the high end of our adopted redshift range, even K_s band fails to probe the NIR stellar bump. To counter this, for sources at redshifts >1 , we additionally use photometry information from the *Wide-field Infrared Survey Explorer* (WISE; Wright et al. 2010) at observed 3.4 and $4.6 \mu\text{m}$ (bands $W1$ and $W2$, probing 1.1 and $1.5 \mu\text{m}$ rest-frame wavelengths at $z = 2$, respectively). We have cross-matched our radio sample, using the positions of the NIR sources, with the All Sky WISE catalog and requiring a 5σ detection in the $W1$ band. Using a matching radius of $6''$ (equal to the PSF size of WISE at $3.4 \mu\text{m}$), we find in total 92 radio sources in the SA22/DXS field with detection in the $W1$ WISE band.

The SED fitting has been done by comparing the observed SEDs of our sample to a set of spectral templates from Bruzual & Charlot (2003, hereafter BC03) stellar population synthesis models. In this work, we use the BC03 model spectra with Padova 1994 evolution track and the Chabrier (2003) initial mass function. After extracting model galaxy spectra, we apply the Calzetti dust attenuation law (Calzetti et al. 2000) for internal dust attenuation and the Madau (1995) law to account for the intergalactic extinction arising by the neutral hydrogen in the intergalactic medium. We allow four metallicity values ($0.2 Z_\odot$, $0.4 Z_\odot$, $1.0 Z_\odot$, and $2.5 Z_\odot$) during the fitting procedure.

As for the SFH, we assume the parametric form of delayed SFHs, which was introduced in Lee et al. (2010) and has been used in previous works to analyze observed galaxy SEDs (e.g., Lee et al. 2014; Wiklind et al. 2014). The function form of this SFH is

$$\Psi(t, \tau) \propto \frac{t}{\tau^2} e^{-t/\tau},$$

where $\Psi(t, \tau)$ is the instantaneous SFR. In this work, we define SFR as the SFR averaged over the recent 100 Myr, instead of instantaneous SFR, based on the reasoning explained in Lee et al. (2009).

The parameter t —which is the time since the onset of the star formation—is allowed to vary from 200 Myr to t_H , where t_H

is the age of the universe at corresponding redshift of each galaxy. τ is varied from 0.1 to 10.0 Gyr with uneven step sizes.

Examples of fits to radio sources' SEDs are shown in Figures 18 and 19. We use the χ^2 output from our SED fitting code to reject fits with χ^2 values above 100 (leading to 54 sources being rejected, $\sim 7\%$).¹⁵ Among sources with acceptable SED fits ($\chi^2 < 100$), $\sim 85\%$ have $\chi^2 < 10$.

4. ENVIRONMENT

In this section, we investigate the small-scale environment of radio sources and more specifically radio AGNs, utilizing both the FIRST and VLA-Deep surveys. We will deal with the following samples (also see Table 2).

1. *FIRST; All*. All cross-matched sources between FIRST and IMS.
2. *FIRST; AGN*. All cross-matched sources between FIRST and IMS, above a radio luminosity limit of $\sim 10^{40} \text{ erg s}^{-1}$.
3. *VLA-Deep; All*. All cross-matched sources between the deep VLA survey and the IMS.
4. *VLA-Deep; AGN*. All cross-matched sources between the deep VLA survey and the IMS, above a radio luminosity limit of $\sim 10^{40} \text{ erg s}^{-1}$.

We start by looking at the Σ_2 and Σ_5 density parameter distributions for the two radio samples. These are shown in Figures 6 and 7. There we plot the distributions of the ratio $\Sigma_{n;\text{radio}}/\Sigma_{n;\text{control}}$, our chosen measure of overdensity. We consider the comparison with both the matched control sample (red filled histograms) and the random control sample (open blue histogram). Focusing first on the total samples (both radio AGNs and star-forming galaxies), we see that the distribution of the overdensity ratio peaks at a value of 1, indicating that the bulk of the sources is found in environments very similar to their matched control sources.¹⁶

The results are markedly different when we consider the comparison with the random field positions. Here we see that the peak of the distribution, for both samples in the case of Σ_2 and for the FIRST sample for Σ_5 , is found at ratios higher than 1, implying that compared to the average field density, radio sources are found predominantly in denser environments. This is not particularly surprising especially since our random field positions are not associated with galaxies and therefore, within the framework of ΛCDM and a hierarchically clustering universe (e.g., Navarro et al. 1997), not associated with a dark matter halo. It is, however, obvious that the distributions of both matched and random control sample overdensity ratios are strongly non-Gaussian. They both exhibit strong high-overdensity tails that extend to environments for radio sources that are up to 100 times denser than those of their control sources. This is reflected in the average overdensity ratio values, also shown for each panel of Figure 6. The calculated skewness of the distribution is well above 0 for all cases. A two-sample Kolmogorov–Smirnov (K-S) test between the random and matched control sample overdensity ratio distributions rejects the null hypothesis that the two samples are drawn from the same parent distribution with high significance.

¹⁵ We checked whether the rejected sources are preferentially found at high radio luminosities, high redshifts, or at more overdense or underdense environments, but this was not the case.

¹⁶ We remind here that the matched control sample matches each radio source with 20–40 sources with similar redshifts, observed J -band magnitude, and rest-frame absolute magnitude color ($M_u - M_r$).

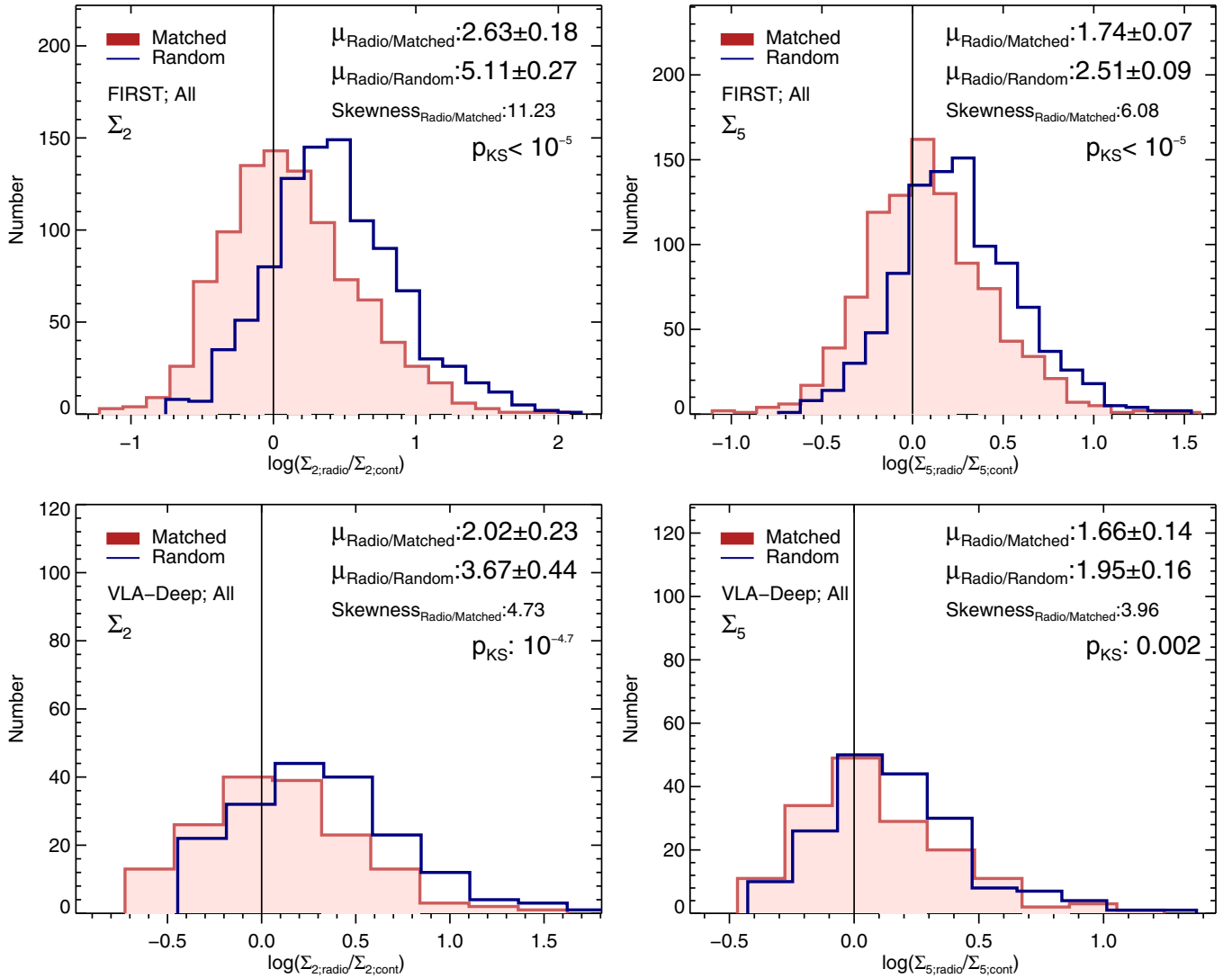


Figure 6. Distributions of the overdensity parameters defined as the Σ_2 (left column) and Σ_5 (right column) ratio between each radio source and its control sample, for all sources in the FIRST (top row) and the VLA-Deep (bottom row) samples. The overdensity ratios for the random and the matched control samples are shown with open blue and shaded red histograms, respectively. The average values for each of the distributions, the skewness of the radio-to-matched overdensity ratio distribution, and the probability p that the two distributions are drawn from the same parent sample are also given for each panel. The vertical line denotes an overdensity ratio of 1, i.e., a radio source resides in an identical environment with its control sample.

(A color version of this figure is available in the online journal.)

If we now focus on the comparison between the two radio samples, FIRST and VLA-Deep, we find that qualitatively their behaviors in terms of both the distribution shape and the average values are the same. However, we note that the degree of overdensity (in terms of highest overdensity ratio and average overdensity ratio) for the FIRST sample appears stronger than for the VLA-Deep. Moreover, the FIRST overdensity distribution appears more heavily skewed to the right. These differences might be driven by the fact that we expect the FIRST sample to include more very bright radio AGNs hosted by massive ellipticals (as was also implied by the redder colors for the VLA-FIRST source observed in Figure 5). This is also corroborated by the radio luminosity distributions of the two radio samples, a larger fraction of the VLA-Deep sources having radio luminosities $< 10^{40} \text{ erg s}^{-1}$.

Finally, it is interesting to compare how the overdensity ratio distribution changes when considering Σ_2 and Σ_5 . One obvious change is that the degree of overdensity appears to dampen as we move to the fifth-closest neighbor from the second-closest

one (e.g., for the FIRST sample the average values for the matched control sample are 2.63 ± 0.18 and 1.74 ± 0.07 for Σ_2 and Σ_5 , respectively). We also see that there is a tendency for the peak of the random control sample overdensity ratio distribution to converge toward a ratio value of 1, with the two distribution peaks coinciding for the case of the Σ_5 for the VLA-Deep sample. This is again qualitatively in agreement with an exponentially declining Navarro–Frenk–White dark matter profile (Navarro et al. 1996), assuming the galaxy distribution to follow the dark matter distribution, together with the predominantly lower-mass galaxies that should dominate the VLA-Deep sample. Finally, we observe that the skewness of the distributions becomes smaller from Σ_2 to Σ_5 , indicating fewer sources in extreme overdensities at large scales.

Let us now turn to the overdensity ratio distributions for the radio AGN subsample of the FIRST and VLA-Deep samples. These are shown in Figure 7 with the same color notation for matched and random control samples as in Figure 6. Most of our observations from Figure 6 also hold true when we only

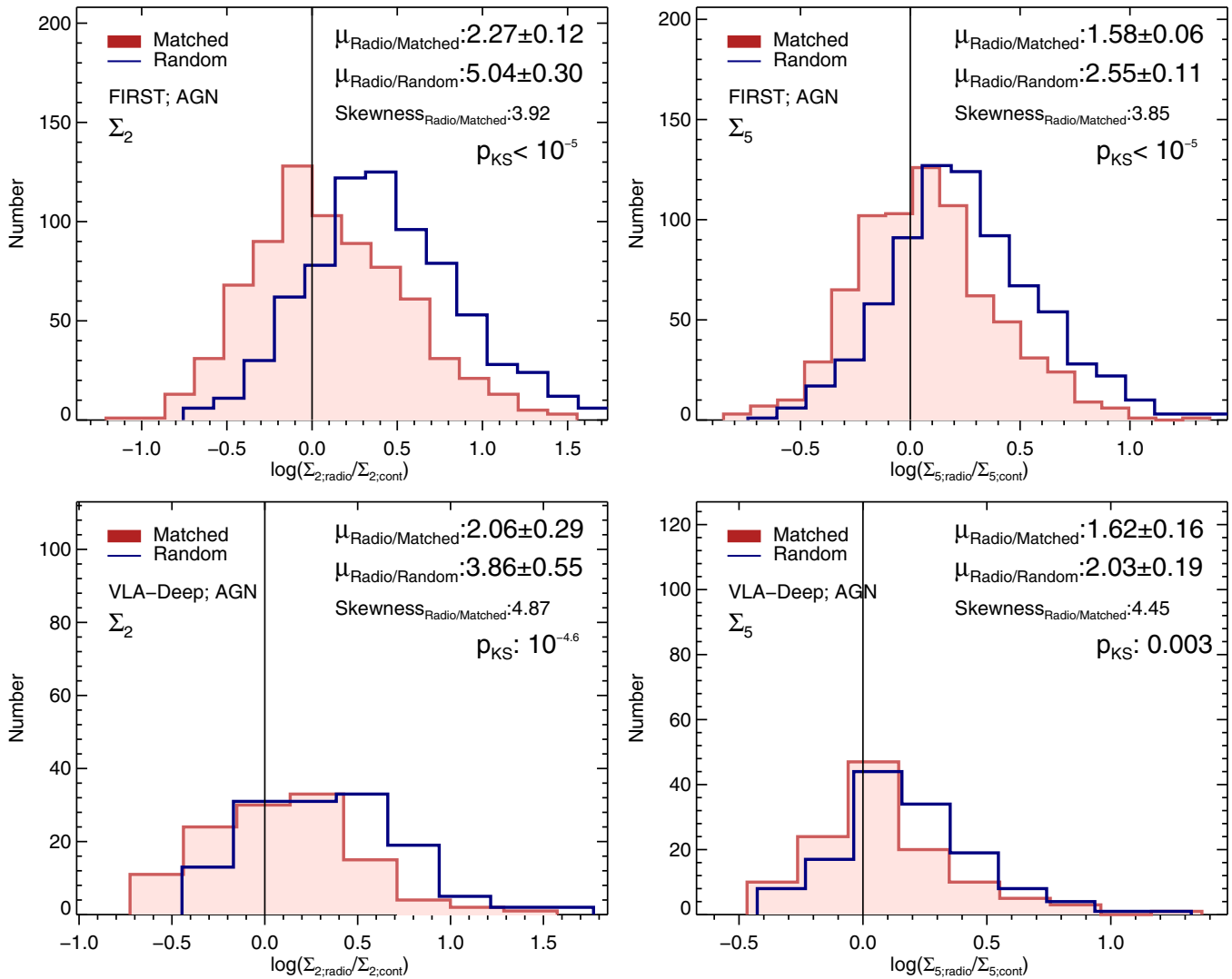


Figure 7. Same as in Figure 6, but now only radio AGNs selected through their 1.4 GHz luminosities are considered. (A color version of this figure is available in the online journal.)

consider the radio AGNs in our samples.¹⁷ There are, however, some additional points of interest. A first comment concerns the fact that the overdensity ratio for the random control sample, for the VLA-Deep sample, seems to be slightly shifted to higher values (in terms of average values) although still within the uncertainty. This may indicate that through our selection we are preferentially picking up more massive galaxies and therefore the difference in environment between these massive galaxies and empty fields becomes wider. However, when we consider the matched control sample, the distributions do not appear to change significantly, with a tendency to actually show slightly lower average values of overdensity ratios and distribution peaks that are shifted toward smaller overdensity ratios (e.g., for the FIRST Σ_2 distribution). This shift may be explained by the fact that we are excluding strong starburst galaxies, which should have radio luminosities right below the assumed AGN luminosity cut ($\sim 10^{40}$ erg s⁻¹). These sources are known to be powered by ongoing mergers and are thus preferentially found in dense small-scale environments. As expected, the two-sample K-S test still rejects the null hypothesis.

¹⁷ We remind that the radio AGN selection is done by means of a radio-luminosity cut, following the local luminosity function of radio sources.

We investigate the significance of the high-overdensity, non-Gaussian tail that is observed for all radio-source samples in Figures 6 and 7. In particular, we want to estimate the probability of this high-overdensity tail to be a chance occurrence. To that end, we draw 10,000 random samples from the total IMS-SA22 sample, each comprising 1000 sources. For each of these random samples we follow the same analysis as described in Section 3, i.e., for each source we assign 20–40 control sources of similar redshift, J magnitude, and $(M_u - M_r)$ rest-frame absolute magnitude color and then calculate the second- and fifth-closest neighbor density parameters for the main and matched control samples. We can then calculate the mean value for the overdensity distribution of each of 1000 samples, as well as its skewness, which is representative of how heavy tailed the distributions are. The distribution of the mean values and skewness values can tell us the probability, and hence significance, of the average overdensities we derived for the FIRST and VLA-Deep samples. The density map of mean overdensity versus skewness value for our Monte Carlo run is shown, together with the individual distributions of the mean overdensity values and skewness values for the 10,000 random samples, in Figure 8.

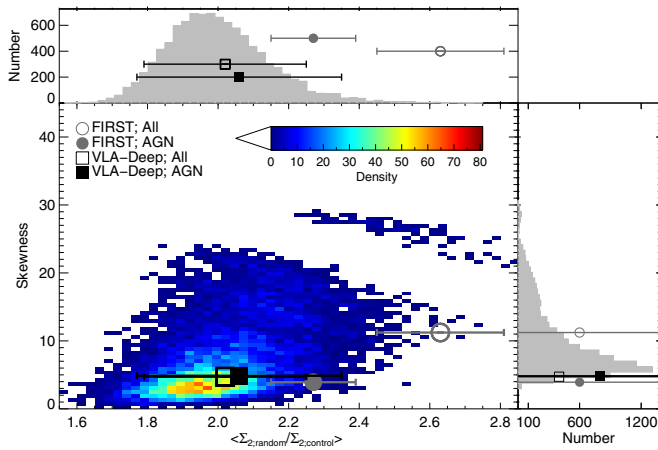


Figure 8. Density map of mean overdensity vs. skewness values resulting from a Monte Carlo simulation with 10,000 runs (central plot). Individual distributions of the average overdensity values and skewness values of the 10,000 samples randomly drawn from the main SA22 sample are also shown (side panels). The corresponding values are shown for the FIRST (gray circles) and “VLA-Deep” (black squares) samples. These samples are further divided into “All” and “AGN” subsamples, shown with open and filled symbols, respectively. Projections of these points on the “Mean Overdensity” and “Skewness” axis are plotted on the side panels.

(A color version of this figure is available in the online journal.)

As can be seen in Figure 8, the distribution peaks at a mean overdensity value of ~ 1.9 and a skewness value of ~ 6 . This implies that, independent of the sample selection, we can expect an average overdensity > 1 with a heavy-tailed distribution. Furthermore, we observe that there is a broad correlation between the mean overdensity and how heavy-tailed the resulting distribution is. Let us now compare these numbers to the mean overdensities calculated for the FIRST and VLA-Deep samples. For the FIRST sources (both full sample and AGN subsample) their mean value is at overdensities well above the peak of the mean overdensity distribution derived. If we take skewness also into account, we see that both the full and AGN FIRST samples are found on the edge of the combined distribution. We calculate the combined probability that a random sample has a mean overdensity value and skewness value equal to or larger than that of the FIRST sample,

$$P_{\text{FIRST};\text{all}} \left[\frac{\Sigma_{2,\text{radio}}}{\Sigma_{2,\text{matched}}} \cap \text{Skewness} \right] = 0.1\%$$

and

$$P_{\text{FIRST};\text{AGN}} \left[\frac{\Sigma_{2,\text{radio}}}{\Sigma_{2,\text{matched}}} \cap \text{Skewness} \right] = 4.4\%$$

for the full sample and the AGN subsample, respectively. On the other hand, the VLA-Deep sample shows a wide range (owing to the small number of sources and hence the large standard error of its mean overdensity value), covering the peak of the mean overdensity distribution of Figure 8. The calculated skewness values for the VLA-Deep samples are close to the peak of the skewness distribution. The combined probability to get such mean values randomly is calculated to be 40.5% and 30.3%, for the full sample and AGN subsample, respectively. We can conclude that while both radio samples appear to inhabit OD environments compared to their control sources, only the FIRST sample appears to do so in a statistically significant manner.

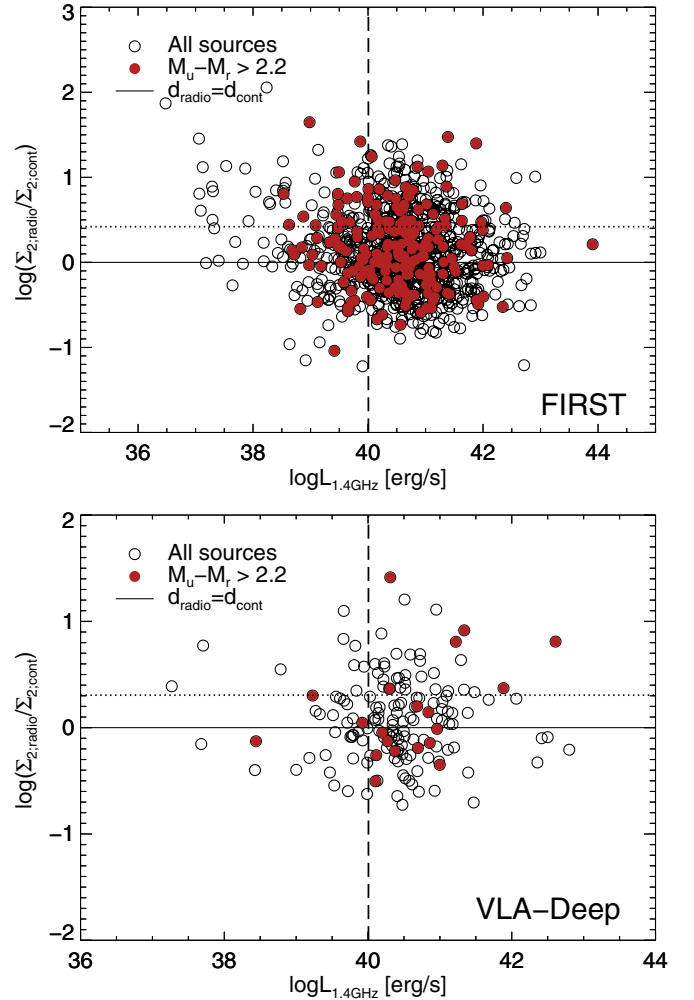


Figure 9. Overdensity ratio parameter, between radio sources and their matched control sources, as a function of radio luminosity at 1.4 GHz for the FIRST (top) and VLA-Deep (bottom) radio sources. The horizontal lines denote a ratio value of 1 (solid line) and the mean overdensity value for the whole sample (dotted line). We also separate sources according to their rest-frame absolute magnitude color ($M_u - M_r$), showing with filled red circles sources with red colors (> 2.2). (A color version of this figure is available in the online journal.)

4.1. Environment and AGN Luminosity

As was discussed in Section 1, galaxy evolution models have been put forth that support the triggering of luminous quasars by gas-rich major mergers (e.g., Hopkins et al. 2006). In addition, evidence has been provided for the most luminous radio AGNs to be also highly associated with ongoing or recent mergers (e.g., Karouzos et al. 2010; Ramos Almeida et al. 2011). Here we test a possible link between the radio luminosity of our radio samples and the overdensity ratios, whose distributions we studied above. This comparison is shown in Figure 9 for both the FIRST (top) and the VLA-Deep (bottom) samples. In addition, in these plots we distinguish between all sources and those that are particularly red (rest-frame absolute magnitude color ($M_u - M_r$) > 2.2). Strateva et al. (2001) showed that local Sloan Digital Sky Survey galaxies with colors $u - r > 2.2$ are mainly early-type, elliptical galaxies with relatively old stellar populations. These should then be the typical “red and dead” galaxies usually associated with bright radio AGNs in the local universe.

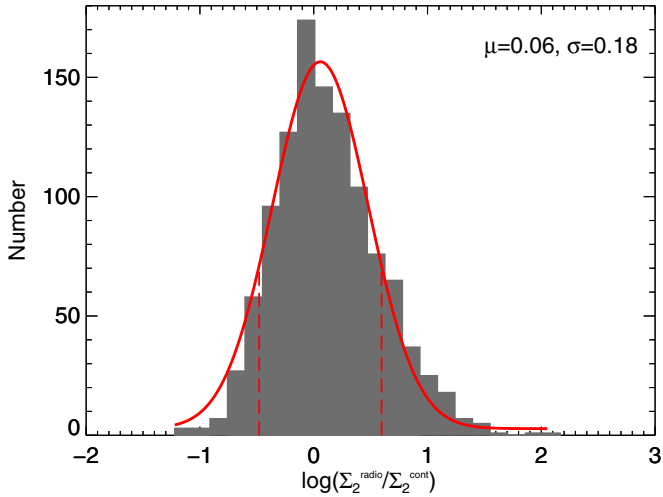


Figure 10. Distribution of the overdensity ratio based on the Σ_2 density parameter for the full combined FIRST and VLA-Deep radio samples. The distribution is fitted with a standard Gaussian profile (shown with the red curve). The mean value and standard error, in logarithmic scale, of the Gaussian are also given. The most underdense and most overdense samples are defined according to the 3 times SE margins shown with the dashed lines on the plot.

(A color version of this figure is available in the online journal.)

We see that both samples do not exhibit any appreciable trend with radio luminosity. We see again that on average they are higher than the ratio-equals-one value (average value shown with the dotted line). However, it seems that on first order the color of these sources does not seem to affect their place on this plot, i.e., red radio sources are not preferentially found in denser environments. We find no evidence for the highest radio-luminosity sources ($>10^{42}$ erg s^{-1}) to be in OD environments either.

Conversely, we note that the low radio-luminosity sources ($<10^{38}$ erg s^{-1}) appear to be preferentially found in OD environments. As star formation should dominate that radio-luminosity regime, this confirms our previous statement that powerful star-forming galaxies are driving the shift of the overdensity ratio distribution peak from Figure 6 to Figure 7.

5. HOST GALAXIES OF RADIO AGNS

In this section, we focus on the properties of the radio AGN host galaxies, derived through SED fitting. For the following we combine the “FIRST, AGN” and “VLA-Deep AGN” samples (i.e., sources with radio luminosities $>10^{40}$ erg s^{-1}). Moreover, as described in Section 3.4, we limit ourselves to the DXS area within the SA22 field, in order to benefit from the uniform K_s -band coverage (see Table 2).

We have shown that while on average most radio AGNs appear to inhabit environments similar to galaxies of similar properties, there does exist a significant subpopulation of radio AGNs that inhabit environments up to 100 times denser than their control sources. We can define two subsamples of radio AGNs that inhabit the most OD and least OD (i.e., most UD) environments compared to their control sources. This separation is done based on the Σ_2 density parameter ratio as we are interested in the close neighbors of radio AGNs. In Figure 10 we show the Σ_2 ratio for the combined FIRST and VLA-Deep samples, which we have fitted with a standard Gaussian profile. Using the derived standard error (SE) of the Gaussian distribution, we define the most OD and most UD subsamples as

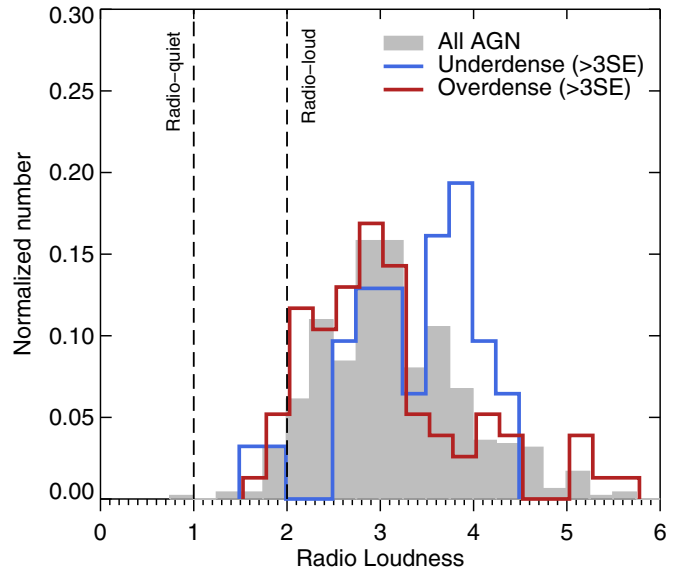


Figure 11. Normalized distribution of the radio-loudness of radio AGNs found in the most overdense (red open histogram) and most underdense (blue open histogram) environments, compared to their control sources. We also plot the distribution for the total luminosity-selected radio AGN sample (gray filled histogram). The limits for radio-loud and radio-quiet sources are shown with dashed lines.

(A color version of this figure is available in the online journal.)

those sources with overdensity ratios above and below the $3 \times$ SE margin with respect to the mean value of the fitted Gaussian.

By defining two samples in terms of the two extremes of the overdensity ratio distribution in Figure 10 and also imposing a radio luminosity limit to select only those sources qualifying as radio AGNs, we can compare the properties of radio AGNs in significantly different environments. For brevity, in the following we shall call these two samples OD and UD, for radio AGNs in the most OD and most UD environments, respectively. We first look at the radio-loudness distributions of the two subsamples. Radio loudness is a measure of the power of the radio jet in an AGN and its dominance over the overall energy output of the nucleus (Kellermann et al. 1989). Prominent radio jets classify an AGN as radio-loud, while radio-quiet sources are thought to lack or have a very weak jet component. Here we use the definition of radio-loudness from Ivezić et al. (2002),

$$R_i = \log \left(\frac{f(1.4 \text{ GHz})}{f(7480 \text{ \AA})} \right),$$

where $\lambda = 7480 \text{ \AA}$ is the central wavelength of the i band in the optical. For both radio and optical fluxes, we use the observed values. Under that definition, we can classify sources with $R_i > 2$ as radio-loud, while for $R_i < 1$ a source is classified as radio-quiet. The R_i distributions of the OD and UD samples are shown in Figure 11.

As expected, most of our luminosity-selected AGNs fall within the radio-loud AGNs, with only a few found in the intermediate regime between radio-quiet and radio-loud limits. Interestingly, we observe that the peak of the R_i distribution of the OD sample is at a value of ~ 3 . The UD sample, on the other hand, shows on average higher values of R_i , with its distribution peaking at ~ 4 . A two-sample K-S test rejects the null hypothesis at a probability value of $p = 0.02$. Conversely, a similar comparison between the radio-luminosity distributions does not reveal any significant differences, with a two-sample

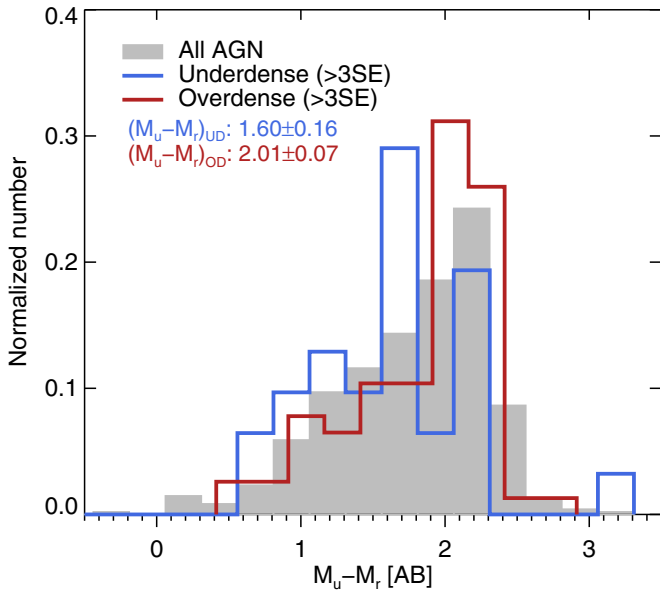


Figure 12. Absolute AB magnitude color $M_u - M_r$ for the UD (blue) and OD (red) subsamples of radio AGNs. The median values of the two distributions are also shown on the plot. For comparison we also plot the normalized distribution of the total luminosity-selected radio AGN sample (gray filled histogram).

(A color version of this figure is available in the online journal.)

K-S test failing to reject the null hypothesis. In other words, radio AGNs in the UD subsample, although more radio-loud, are not more luminous in the radio compared to their OD counterparts.

We now turn our attention to the host galaxy properties of the two subsamples. In Figure 12 we plot the rest-frame absolute magnitude color ($M_u - M_r$) for the UD and OD subsamples. As discussed previously, the ($M_u - M_r$) color should cover the 4000 Å break and therefore reflect the age of the dominant stellar populations in these galaxies, as well as trace potential ongoing star formation. We observe that for the OD sample the majority of sources are found at a color of ~ 2 , while sources in the UD sample have a wider spread, reaching the bluest colors. A comparison between their median colors reflects this difference. This is further corroborated by a value $p = 0.001$ derived from a two-sample K-S test. While our sample covers a significantly wider redshift range, the differentiation between the two subsamples in terms of their rest-frame ($M_u - M_r$) color, together with the findings by Strateva et al. (2001), implies a difference in host galaxy morphologies and SFHs.

We can use the results of our SED fitting to calculate the star formation efficiency of the radio sources in the OD and UD subsamples. The SFR per unit of stellar mass, the specific SFR or sSFR, can be used as a measure of the star formation efficiency. We plot the sSFR of the two subsamples as a function of their redshift in Figure 13. In particular, we want to compare these to the known “main sequence” (e.g., Rodighiero et al. 2010; Elbaz et al. 2011) of star formation, on which normally star-forming galaxies lie at a given redshift. This is shown with the solid line in Figure 13, with the dashed lines showing the 3σ margins of the “main sequence.” Sources above the upper dashed line in the same plot are considered to be vigorously star-forming galaxies (starbursts), while sources below the lower dashed line are usually red ellipticals, with zero or minimal ongoing star formation (both dashed lines and source classification taken from Elbaz et al. 2011). As we can see, the radio AGNs are found both above and below the “main sequence.” We

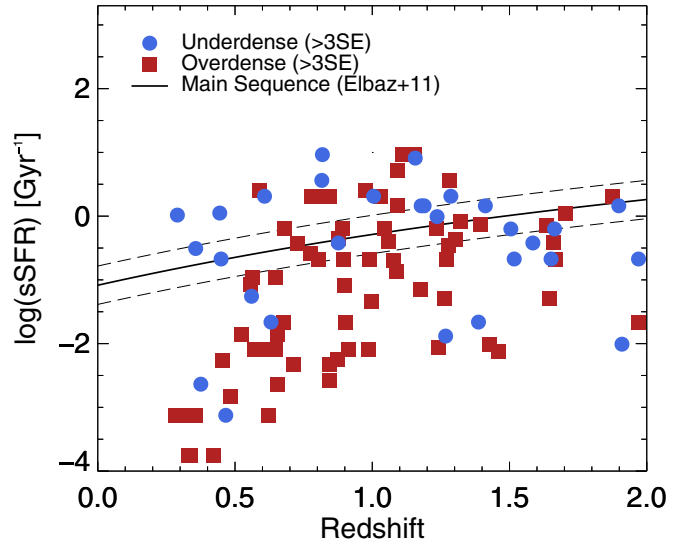


Figure 13. Specific SFR as a function of redshift for the two subsamples of radio AGNs, OD (red) and UD (blue). The average sSFR values of the matched control sample are also shown (with open blue and red circles for the UD and OD samples, respectively). The solid black line shows the calculated “main sequence” of star formation, as reported in Elbaz et al. (2011), while the dashed black lines show the 3σ margins of that relation.

(A color version of this figure is available in the online journal.)

observe, however, that radio AGNs in the UD subsample are preferentially found around or above the “main sequence,” while the bulk of the OD radio AGNs are found below it.

We investigate this further in Figure 14, where instead of individual sources, median values over redshift bins are plotted. We take an additional number of measures to ensure that bad SED fits and contamination from a strong optical AGN component do not affect our results. For the median values, we constrain ourselves to sources with

1. detections in at least five of our total seven photometric bands (seven out of nine, in the cases where *WISE* photometry is used);
2. low χ^2 values for their photometric redshift fits ($\chi^2 < 1000$ ¹⁸);
3. photometric redshift with χ^2 from the galaxy template fit lower than the χ^2 from the AGN template fit; and
4. low χ^2 values for their broadband SED fitting (as already explained in Section 3.4).

The above additional restrictions, while further reducing the number of sources from which we draw conclusions, err on the side of caution. We want to ensure trustworthy SED fitting results, both in the sense of accurate photometric redshifts and minimizing any AGN contamination that would affect our estimation of the sSFR of a source. We can now directly compare between the two subsamples of radio AGNs. We can see that there is a significant difference between the two subsamples, in terms of their sSFR, below redshift ~ 1 . At higher redshifts, while the same trend for UD radio AGNs to show higher sSFR compared to their OD counterparts persists, it is not significant. We can see how the definition of the UD and OD samples affects our results. We shift our selection limit of the two subsamples from 2.5 times, to 3 times, to 3.5 times the SE (shown in the left, middle, and right panels of Figure 14, respectively).

¹⁸ We have looked at the fraction of outliers and σ_{NMAD} as a function of the χ^2 cutoff. However, both of them show a very weak, if any, dependence on the χ^2 .

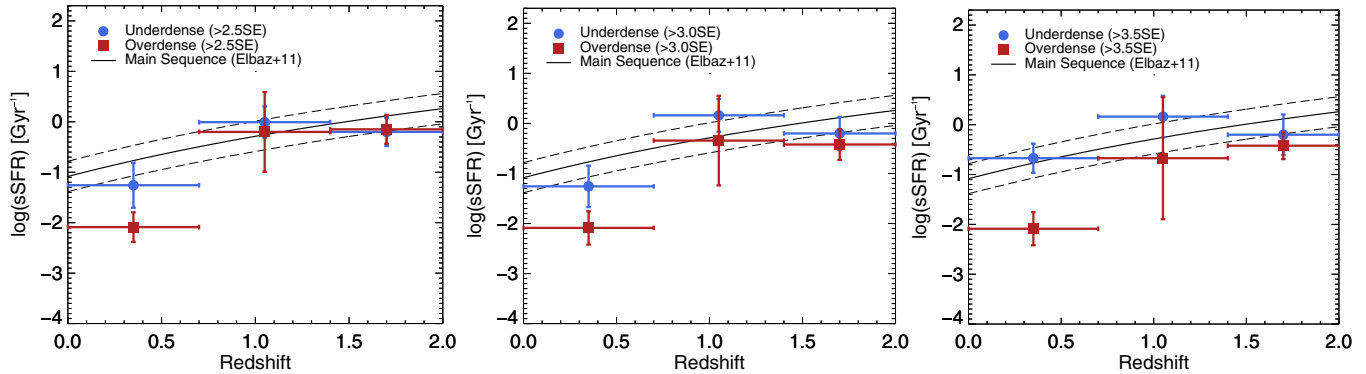


Figure 14. As in Figure 13, the sSFR is plotted as a function of redshift for the two subsamples of radio AGNs, OD (red) and UD (blue), but in redshift bins. The solid black line shows the calculated “main sequence” of star formation, as reported in Elbaz et al. (2011), while the dashed black lines show the 3σ margins of that relation. From left to right, the selection limit for overdense and underdense sources changes from 2 times (left), to 3 times (middle), to 3.5 times the SE (right). For all panels, the radio AGNs found in the most underdense environments show on average higher sSFR than those in the most overdense environments. This is particularly significant at redshifts < 1 .

(A color version of this figure is available in the online journal.)

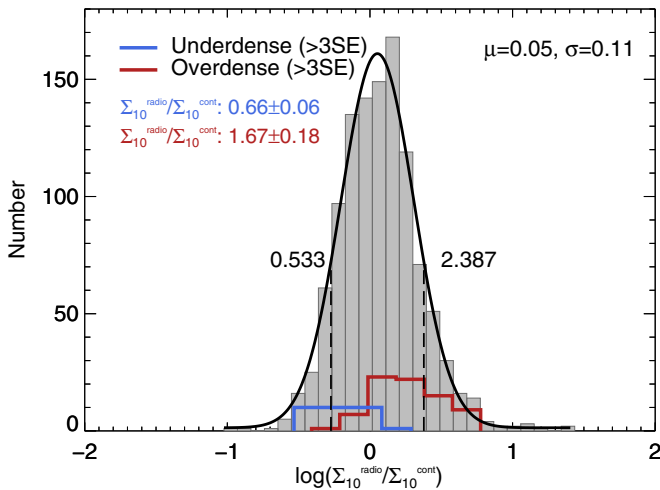


Figure 15. Distribution of the overdensity ratio based on the Σ_{10} density parameter for the full combined FIRST and VLA-Deep radio samples (filled gray histogram). The distribution is fitted with a standard Gaussian profile (shown with the black curve). The mean value and standard error, in logarithmic scale, of the Gaussian are also given. We also mark the 3 times SE margins for the Gaussian profile (dashed lines). The distributions of the overdensity ratio of the UD and OD subsamples¹⁹ of radio AGNs are also shown (in blue and red open histograms, respectively), together with their median overdensity ratio values.

(A color version of this figure is available in the online journal.)

It is clearly seen that the gap in sSFR between the two subsamples grows wider as the contrast in the overdensity ratio between the two subsamples increases.

As we are doing our selection based on the environment overdensity of these radio AGNs, the effect seen in Figures 13 and 14 may just reflect differences in the large-scale environment of these sources. A systematic difference between the star formation properties of galaxies in the field and in cluster environments is known to exist (e.g., Blanton & Moustakas 2009; Peng et al. 2010; Alberts et al. 2014). Therefore, it is conceivable that the same radio AGNs that show the higher small-scale overdensities are also embedded in larger-scale overdensities and hence exhibit quenched star formation due to their large-scale environment.

We test this in Figure 15, where the overdensity ratio (defined as the ratio of the density around a radio source and the average density around its matched control sources)

based on the 10th-closest neighbor is plotted for the whole radio sample. Unlike for the second-closest neighbor, the 10th-closest-neighbor overdensity ratio should reflect the large-scale environment properties of these sources. We follow the same exercise as before to define the 3 times SE margin of the distribution. As a next step, we overplot the Σ_{10} overdensity ratio distributions for the UD and OD radio AGN subsamples (in blue and red open histograms, respectively). It becomes immediately obvious that the bulk of these radio AGNs are not found in the most OD large-scale environments. In fact, the median overdensity ratio values of the two subsamples are both within the 3 times SE margins of the full sample distribution.

6. DISCUSSION

Let us summarize briefly the main findings of our study.

1. The bulk of the radio sources, for both the FIRST and VLA-Deep samples, appear to inhabit environments that are very similar to their matched control sources (Figure 6). Conversely, when matched to random field positions, they exhibit strong overdensities.
2. There is a component of radio sources that is found in the most dense environments, exhibiting densities up to 200 times that of their control sources. The same holds true if we consider just the luminosity-selected radio AGNs (Figure 7).
3. The average overdensity ratio value for the FIRST sample is significantly above 1 with a very low probability for this to be a chance result (2.62 ± 0.18 with a chance probability of 0.1% and 2.27 ± 0.12 with a chance probability of 5.3% for all radio sources and just radio AGNs, respectively). While for the VLA-Deep sample the average overdensity ratio is also above 1, it is not significantly so (Figure 8).
4. We find no correlation between the radio luminosity of a source and its small-scale environment. This holds true for both all sources and just radio AGNs, up to the highest radio luminosities probed here (10^{44} erg s^{-1} ; Figure 9).
5. Radio AGNs in the most UD environments exhibit, on average, higher radio-loudness and bluer ($M_u - M_r$) colors than then most OD radio AGNs (Figures 11 and 12, respectively).
6. Radio AGNs in the UD subsample show, on average, higher sSFRs compared to radio AGNs in the OD subsample,

at or above the “main sequence” of star formation. This difference is more prominent at redshifts <1 , although it persists even out to redshift ~ 2 , albeit at lower significance (Figure 14).

7. The UD and OD subsamples of radio AGNs do not correspond to the most UD and OD large-scale environments, as probed by the 10th-closest-neighbor overdensity ratio (Figure 15). Their sSFR differences cannot thus be attributed to large-scale environment quenching.

6.1. Possible Shortcomings of the Analysis

Before we continue with the comparison with previous studies and the discussion of the above summarized results, we wish to investigate possible biases and systematical effects that may influence our results. These can be broadly divided in terms of our selection and in terms of our analysis. We will discuss each of the two separately.

6.1.1. Selection Effects

Our main selection is done in the radio, 1.4 GHz, and the NIR, J band. Radio selection, especially at lower frequencies, tends to pick up either star-forming galaxies (owing to their relatively steep spectrum) or radio-quiet AGNs at low radio luminosities, starburst galaxies and weak radio AGNs at intermediate radio luminosities, and AGNs with powerful radio jets at the highest radio luminosities. Here we have combined two different radio surveys, one shallow but wide and one deep that however focuses on a small area on the sky. As such, we can efficiently probe down to at least 0.1 mJy (the 5σ limit for the B-configuration VLA-Deep observations), effectively including many star-forming and composite (star formation + AGN) galaxies in our sample (e.g., Seymour et al. 2008).

We assume a radio luminosity cut in order to select radio AGNs and study their environment. At radio luminosities $>10^{40}$ erg s $^{-1}$ the sky is dominated by radio AGNs rather than star-forming galaxies (e.g., Best et al. 2005b; Mauch & Sadler 2007). We expect a contamination from star-forming galaxies in our luminosity-selected radio AGN sample of $<10\%$. While our radio luminosity limit for AGN selection is based on the local radio luminosity function, it is expected that, as a result of the evolution of the luminosity function of both AGNs and star-forming galaxies with redshift, this limit should shift toward higher values at earlier epochs. However, owing to the redshift–luminosity relation imposed by the flux-limited nature of our sample, we do not expect a significant effect in our selection.

Owing to the flux limit of our radio observations, we are by definition missing fainter radio sources. As has been shown (e.g., Seymour et al. 2008; Padovani et al. 2009) at flux densities below 1 mJy, the sky is increasingly dominated by star-forming galaxies and potentially radio-quiet AGNs. As such, we do not expect to be missing a significant component of radio AGNs from our study, especially out to our relatively modest assumed redshift limit.

We combine the radio selection with a magnitude-limited sample in the NIR from IMS. As such, our secondary selection is in J band, at $\sim 1.2\mu\text{m}$. This is the longest wavelength available over the full area of IMS in the SA22 field and hence the least prone to obscuration. Furthermore, for radio sources at low and moderate redshifts (<0.5), J band probes the light in the NIR, which should be dominated by emission from old stellar populations. We know that radio AGNs are usually found in massive galaxies (e.g., Best et al. 2005a),

and therefore we do not expect our results to be severely affected by the exclusion of low-mass galaxies. Another factor we need to consider is contamination of the J -band light from powerful AGN emission. This is particularly relevant for the most luminous AGNs, quasars, which are usually point-like and whose whole SED is dominated by their nuclear emission. The maximum optical luminosity of our sources (in i band) is below 10^{46} erg s $^{-1}$ and therefore well below the bright quasar luminosity regime ($>10^{47}$ erg s $^{-1}$). Only 19 sources in our sample exhibit optical luminosities $>10^{45}$ erg s $^{-1}$, the nominal limit above which quasars dominate over their host galaxy emission (e.g., Shen et al. 2011). Therefore, there should not be significant contamination (mainly in terms of the control sample selection) from AGN emission in the optical and NIR.

6.1.2. Methodology Caveats

There are two main points that can introduce uncertainties and systematics to our results: (1) the estimation of photometric redshifts and (2) the fitting of the broadband SEDs and the derivation of stellar masses and SFRs for galaxies. As we showed in Section 3, we have taken a number of steps usually employed in studies of photometric redshifts to minimize the effects of photometric uncertainties and also calibrate photometric redshifts to an accurate set of spectroscopic redshifts. We have further showed that for the majority of radio sources with spectroscopic redshifts, the estimated photometric redshifts agree well within 15%. We calculated the fraction of miscalculated redshifts for our radio sources (in terms of outlier fraction) to be $\sim 10\%$. This translates to a roughly 10% uncertainty of the calculated fraction of AGNs in OD or UD environments. Given that there is no preferential bias in the miscalculated photometric redshifts (i.e., we see in Figure 3 that of the two radio-source outliers, one exhibits higher and one lower photometric redshift compared to their true redshifts), we do not expect a systematic effect on our results. Moreover, Figure 3 is based on VVDS data, and therefore all sources included have an optical magnitude of at least 22.5 AB. As most of our radio sources are actually fainter than this limit and it is known that at lower optical magnitudes the potential contamination from a powerful nucleus is smaller, we expect the outlier fraction calculated from Figure 3 to be a conservative upper limit. In reality, we expect lower optical luminosity radio sources to exhibit more accurate photometric redshifts.

We showed that the uncertainty of our photometric redshifts for the main sample is 0.038. This means that the width of the redshift slices used for the calculation of the environment density parameters, $\pm 0.1(1+z)$, is $>2.5\sigma$ of the photometric redshift. Finally, as our overdensity parameters are expressed in terms of a density ratio between each radio source and its control sources, any potential systematic effects induced by the photometric redshifts will cancel out.

The second point we need to consider is possible problems with the results of our SED fitting. Assuming accurate redshifts and relatively low contamination from the nuclear emission (both points covered previously), the next pitfall that need be considered is possible degeneracies between the different parameters of the fit and the accuracy of the properties derived, i.e., how well can the stellar mass and SFR be constrained. As was discussed previously, the NIR emission is necessary to estimate the stellar mass of a galaxy. Given our redshift range ($z < 2$) and the fact that we require full NIR coverage to perform the SED fitting (i.e., up to $2.2\mu\text{m}$ for $z < 1$ and up to $4.6\mu\text{m}$ for

$z > 1$), we are confident in our estimation of the stellar masses (e.g., Shapley et al. 2005; Lee et al. 2009).

The calculation of absolute SFRs is not as straightforward. Owing to the dusty nature of the birthing sites of stars, a large fraction of young stellar emission is absorbed and reradiated in the mid- and far-infrared regime. As such, we are at a disadvantage with our current data set missing any data points above $2.2 \mu\text{m}$ ($4.6 \mu\text{m}$, respectively). Karouzos et al. (2014a) showed that in absence of far-infrared data, SFRs in radio AGNs can be underestimated by at least an order of magnitude. However, it is important to note here that SFRs are used in our study to compare the different subsamples of UD and OD radio sources, and therefore this difficulty in calculating absolute SFRs should not affect us severely. Furthermore, given our selection, we do not expect significantly different dust properties between the UD and OD subsamples. This implies that the missing component of “hidden” star formation should not be preferentially larger for one of the two subsamples.

6.2. Comparison with Other Studies

6.2.1. Environment of Radio AGNs

A direct comparison can be drawn between this study and our previous study on the environment of radio AGNs (Karouzos et al. 2014b). We have improved on that work in two key aspects: we have done a more vigorous control sample selection (introducing the color matching), and we have expanded the radio luminosity range probed by at least two orders of magnitude (maximum luminosity probed here is $\sim 10^{44} \text{ erg s}^{-1}$, compared to the $\sim 10^{42} \text{ erg s}^{-1}$ previously). In addition, we have expanded on previous works to look at the host galaxy properties, differentiating between those radio AGNs in the most OD and most UD small-scale environments.

Our key results in terms of the environment properties of radio AGNs match very well with those from Karouzos et al. (2014b), essentially showcasing the relatively ordinary environments that the bulk of radio AGNs reside in. The average overdensity ratios found here match remarkably well with those for the similar luminosity-selected radio AGN sample of Karouzos et al. (2014b). The only exception to that is the overdensity ratio for the Σ_2 density parameter, where the VIDEO results give a significantly higher value (5.4 ± 1.3 compared to 2.27 ± 0.12 for this study). This difference might arise as a result of the different (and more vigorous) matching criteria used here for the selection of the control sources. A better matching in terms of the host galaxy properties of the radio AGNs to their control sample, under the assumption that radio AGNs on average do not inhabit different environments than their nonactive counterparts, would lead to a decreased mean overdensity ratio.

A mean overdensity of radio AGNs above 1 also agrees well with previous studies of the environment of radio AGNs by Best (2004), Tasse et al. (2008), Donoso et al. (2010), Bradshaw et al. (2011), Lietzen et al. (2011), van Velzen et al. (2012), Ramos Almeida et al. (2013), Worpel et al. (2013), and Pace & Salim (2014). We should note, however, that each of these studies has followed a different way of both selecting their radio sample and defining their control sources. As a result, both the host galaxy stellar mass and radio AGN luminosity ranges probed are different for each one of these studies. Moreover, they all use different measures of environment overdensity. Therefore, a direct comparison is difficult. However, there appears to be a consensus that, especially at small scales ($< 1 \text{ Mpc}$), radio AGNs

are on average embedded in denser environments than galaxies of similar mass, color, and morphology.

Despite our expanded radio luminosity range, the absence of any appreciable trend between the AGN radio luminosity and its environment overdensity persists. This may be somewhat puzzling and in contrast to prevalent models of powerful AGN triggering through mergers. It is in line with the results of Karouzos et al. (2014b) and also in good agreement with the study of Villforth et al. (2014). Ramos Almeida et al. (2011), however, showed that up to $\sim 90\%$ of their sample of powerful radio AGNs (2 Jy sample) shows morphological distortions, signs of recent mergers, much more than their control sample. Given the radio brightness of these galaxies and the fact that the majority of them show optical emission lines, this may indicate a different flavor of AGNs than the ones we are dealing with here.

6.2.2. Environment and Host Galaxies

The host galaxies of radio AGNs have been studied intensively, in terms of both their morphologies and the stellar populations that they host (e.g., Best et al. 2005a). It is now believed that there is a fundamental division within the general population of radio AGNs, driven mainly by the accretion rate onto their central supermassive black holes, classifying them into high- and low-excitation radio AGNs (e.g., Hardcastle et al. 2007). In turn, this classification reflects the different modes of gas feeding toward the nucleus of these galaxies. The latter type of radio AGNs are believed to be fed through hot gas, have low accretion rates, and exhibit weak or no optical emission lines. The former type, on the other hand, exhibits strong optical emission lines, implying efficient accretion. It has been found that this dichotomy in feeding is also accompanied by a dichotomy in host galaxy properties, with high-excitation radio AGNs being characterized by relatively young stellar populations and ongoing star formation. This is in contrast to their low-excitation counterparts, which show old stellar populations (e.g., Herbert et al. 2010; Best & Heckman 2012; Hardcastle et al. 2013).

A connection between the above and the environments of radio AGNs has been attempted in previous studies. Tasse et al. (2008) argued that low-excitation radio AGNs live in overdensities and are being fed by the ample intercluster gas available in such environments. On the other hand, low-mass, high-excitation radio AGNs are found in large-scale underdensities hinting toward close pair interactions driving the triggering of these AGNs. This is somewhat corroborated by the study of Ramos Almeida et al. (2013), which finds galaxies to show a smaller degree of spatial clustering around strong-lined (high-excitation) radio AGNs compared to their weak-lined (low-excitation) counterparts. In our study we make a link between the environment of radio AGNs and star formation in their host galaxies. Our finding that radio AGNs in the densest small-scale environments show the lowest sSFR and relatively moderate power jets is in agreement with the findings by Ramos Almeida et al. (2013), as these sources should be the equivalent of weak-line radio AGNs. As expected, these sources have low sSFR and are expected to be mainly fed by the accretion of hot gas from their halo.

On the other hand, radio AGNs with high sSFR and high-power jets (as exhibited by their radio-loudness distribution) may be triggered by mergers, as is implied by Ramos Almeida et al. (2013) for their sample of radio AGNs with recent star formation activity (based on results by Dicken et al. 2012) and further corroborated by the results of high spatial clustering

around these galaxies in their study. Our results, however, may point toward a different direction. We showed that these sources exhibit high sSFR, on par with or above the “main sequence,” but at the same time are found in the most UD small-scale environments within our sample. This would discard close pair interactions and mergers as the driver of nuclear activity in these sources. Moreover, we showed that, on average, these most UD sources at small scales live in unremarkable large-scale environments. This therefore also rejects the possibility that cooling flows (e.g., Fabian 1994) within a cluster environment are responsible for the ongoing star formation and triggering of the radio AGNs. This population of UD radio AGNs may be related to the low optical luminosity radio-loud quasars found to show a star formation excess, compared to their radio-quiet counterparts, by Kalfountzou et al. (2014). The authors find that radio-loud quasars at optical luminosities $< 10^{45.5}$ erg s $^{-1}$ show an excess of star formation (as reflected by the far-infrared properties), on average lower dust temperatures, and potentially higher dust masses.

6.3. How to Trigger a Radio AGN?

We have shown evidence that the environments of radio AGNs are not particularly different from those of nonactive galaxies with similar properties (in terms of both their masses and SFRs). Nevertheless, we find a significant subpopulation of radio AGNs that do appear to inhabit very dense environments at small scales. For these galaxies, close pair interactions and galaxy mergers might be important for the triggering of the active nucleus. How can we then differentiate between the different processes responsible for triggering these radio AGNs?

The star formation properties of radio AGNs in the most and least dense environments might be able to provide the necessary clues. As it became apparent from our comparison with previous studies in the literature, while radio AGNs are predominantly believed to reside in somewhat OD environments, what this means in terms of their triggering is heavily debated. Below we address two different aspects of this problem before attempting to draw a single consistent picture.

1. *Jet power.* We do not have a clear picture of what drives the power of radio AGN jets. A dense gas screen with which the jet can interact can lead to increased radio emission. Such would be the case of radio AGNs residing in rich clusters with dense intracluster medium. Alternatively, the spin of the jet-producing supermassive black hole may also play a role in how powerful a jet is. Our understanding of spin processes is very poor, although semianalytic models imply that galaxies with rich merging histories (as is the case, for example, for central cluster galaxies) may host more rapidly spinning supermassive black holes (e.g., Fanidakis et al. 2011).
2. *AGN power.* We know that the availability and the temperature of gas in galaxies decide the power of a triggered AGN. Efficient accretion of cold gas, either through a cooling flow (in a cluster where radio AGN feedback has not kicked in), through a gas-rich merger (in group environments), or from mass loss of young stars and along cold filaments (in any environment), can trigger powerful AGNs with Eddington accretion ratios close to 1. On the other hand, inefficient hot gas accretion, either from the intracluster medium (in cluster environments) or from the galaxy’s own halo (in “normal” environments), leads to low-luminosity AGNs with low (< 0.1) accretion ratios.

We propose that the existence of a population of radio AGNs in UD environments compared to their control sources with high sSFRs and high radio-loudness offers compelling evidence for triggering through stellar feedback (e.g., Norman & Scoville 1988). As we explained above, their UD environments discard mergers and galactic interactions as the dominant effect for triggering these systems. Moreover, their “normal” large-scale environments also preclude an important role of hot or cold gas accretion from a cluster environment. Cold gas accretion along filaments, which can extend to large scales (e.g., Kereš et al. 2005), has been argued to provide galaxies with a significant part of their cold gas reservoir. However, as Kereš et al. 2005 has shown, this mode of gas accretion is particularly relevant for galaxies at mass $M_{\text{stel}} < 10^{10.3} M_{\odot}$. Both the UD and OD subsamples have mean stellar masses above that limit, with most sources of both samples at $M_{\text{stel}} > 10^{10} M_{\odot}$. We thus do not expect accretion along cold filaments to be a viable feeding mechanism for the majority of these radio AGNs. On the other hand, the presence of ongoing vigorous star formation offers a gas reservoir that can be tapped into to trigger an AGN. In particular, it has been shown that mass-loaded winds from relatively low mass stars in their asymptotic giant branch phase can dominate the mass outflow during intense episodes of star formation (e.g., Winters et al. 2003; Wild et al. 2010) and can lead to the triggering of an AGN, albeit with a certain time lag (e.g., Davies et al. 2007; Wild et al. 2010). The last missing piece of the puzzle may come from the difference of the radio-loudness distribution of these sources. Systems that are experiencing intense star formation that may be feeding the central AGN are expected to have high degrees of obscuration (e.g., Wild et al. 2007). This would lead to a decreased optical emission and therefore a shift of their radio-loudness toward higher values compared to the relatively unobscured radio AGN counterparts residing in dense environments. Additionally, radio luminosities of the UD radio AGNs may be contaminated by their ongoing SF, which should also contribute to the total radio emission measured by the large VLA beam, over the whole galaxy.

It is important to note here that Figure 14 not only shows a difference in sSFR between the UD and OD subsamples but also implies a redshift evolution of this apparent subdivision among radio AGNs. Above a redshift of $z \sim 1$ the two subsamples appear to be consistent with each other (within the measured uncertainties). Moreover, the OD sample shows higher sSFR compared to $z < 1$, consistent with normally star-forming galaxies at similar redshifts. This reflects the expected evolution of the dominant triggering mechanism with redshift. Moreover, it agrees well with the general trend for any environmental dependence of star formation in galaxies to wash out at redshifts > 1 (e.g., Scoville et al. 2013).

We are now ready to outline a scheme of how radio AGNs can be triggered. In the local universe it seems that the availability of gas is the controlling factor that drives differences between different flavors of radio AGNs. Radio AGNs embedded within dense environments, either small or large scale, are fed through accretion of hot gas either from their own halo or from the intracluster medium, respectively. These are the low-excitation radio AGNs mentioned before, and they exhibit low sSFRs, well below the “main sequence” of star formation. On the other hand, we have radio AGNs found in the most underdense environments (UD subsample), whose activity should be unrelated to their environments. The high sSFRs exhibited by these sources imply that the ongoing star formation might provide the necessary

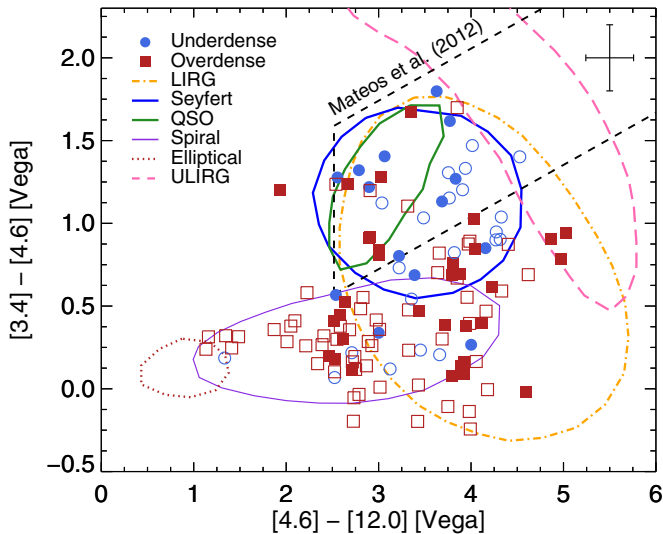


Figure 16. *WISE* color–color plot for the 3.4, 4.6, and 12 μm bands. We show sources in the UD (blue circles) and OD (red squares) sub-samples of radio-AGN. We separate sources that are detected in the longest wavelength band (12 μm ; filled symbols) from those with only upper limits (open symbols). The loci of different types of astronomical objects are taken from Wright et al. (2010) (solid lines). The dashed line shows the AGN selection locus from Mateos et al. (2012). The typical uncertainty of the measurements is shown in the upper right corner of the plot.

(A color version of this figure is available in the online journal.)

fodder for the central supermassive black hole. These are the termed high-excitation AGNs.

The situation at higher redshifts appears to be different, as potentially gas-rich mergers and more readily available cold gas within galaxies shift accretion in radio AGNs toward a more efficient mode, accompanied by ongoing star formation. We therefore observe a much less significant difference not only of the environment but also of the star formation properties of these sources.

6.4. An Infrared Point of View

Mid-IR colors can be used to differentiate between different flavors of AGNs. Gürkan et al. (2014) showed that the *WISE* luminosity at 22 μm and luminosity ratio between 22 and 3.4 μm (*WISE* bands *W4* and *W1*, respectively) can be used as a proxy for Eddington accretion ratio and can thus be used to differentiate between low and high accretion rate radio AGNs. To get the maximum number of radio sources with *WISE* information, we performed a match between our total radio sample and the All Sky *WISE* catalog (containing detections above 5σ) and the All Sky *WISE* Reject table (containing detections below 5σ). The cross-matching was done in the same manner as described in Section 3.4. We find in total 759 radio sources in the SA22 field with detection in at least one *WISE* band at the 3σ sensitivity limit. In addition, we also find 32 matches with lower-significance detections. Assuming the latter to be upper limits, we use a total of 791 SA22 radio sources to calculate the luminosity ratio between 22 and 3.4 μm .

In Figure 16, we show the (4.6–12) μm and (3.4–4.6) μm color–color plot for the UD and OD subsamples of radio AGNs. We see that the two subsamples occupy distinct regions of the *WISE* color parameter space. Radio AGNs in the UD subsample are mainly contained within the locus of Seyfert galaxies, with relatively red (3.4–4.6) μm colors of ~ 0.8 . On the other hand, OD radio AGNs are mostly found inside the spiral and luminous

infrared galaxies loci, with only a few consistent with AGN colors. The AGN selection by Mateos et al. (2012) mostly picks up radio AGNs in the UD subsample but largely misses radio AGNs in the most OD environments.

The distinction between the UD and OD radio AGNs in our sample becomes even clearer in Figure 17. In this plot we show the distribution of the 22 μm to 3.4 μm luminosity ratio distribution for the two subsamples below (left panel) and above (right panel) a redshift of $z = 1$. For a redshift $z < 1$, where a significant difference in sSFR is observed between the UD and OD sources, we also see that their *WISE* luminosity ratio distributions are significantly different. While OD sources show a distribution peaked at ratio values of ~ 2 , the UD sources show a double-peaked distribution, with the first peak at around a ratio of ~ 1 and a second broad peak at around a ratio values of ~ 10 , while extending to much higher ratios than their OD counterparts. A two-sample K-S test gives a $p = 0.03$.

If we now turn to the same distribution but for sources at redshifts $z > 1$ (right panel of Figure 17), the differences between OD and UD sources become smaller, with the peak of the UD distribution remaining at a ratio value of ~ 10 but the peak of the OD distribution shifting to a ratio value of ~ 5 . Furthermore, both distributions are missing the low-value tails and both extending to the highest luminosity ratio values within their parent sample. A two-sample K-S test fails to reject the null hypothesis at high significance. We note here that, while the OD sources show lower luminosity ratio values, they still have ratios that are high compared to the low-excitation radio AGNs from Gürkan et al. (2014). Figure 16 implies that the mid-IR emission of the OD radio AGNs may be dominated by their stellar component, rather than the AGNs. Therefore, the red histograms of Figure 17 may be actually overestimating the Eddington ratios of these sources. This can reconcile our OD radio AGNs with the low-excitation radio AGNs of Gürkan et al. (2014).

Nevertheless, we can conclude that sources in the most UD environments and with high sSFRs also show on average higher accretion rates, typical of efficient accretion of cold gas. This is in agreement with the scenario put forth above and matches with the far-IR properties of low optical luminosity radio-loud quasars of Kalfountzou et al. (2014).

7. CONCLUSIONS

We have used data from the new IMS NIR survey of the VIMOS-SA22 field together with data from the DXS survey within the same field to study the environment and host galaxy properties of radio sources over a wide dynamic range of radio luminosities and environments. In particular, we have focused our investigation on the small-scale environment of these sources, showing that the majority of radio sources are found in environments consistent with the environments of sources with similar *J*-band magnitude, redshift, and rest-frame absolute magnitude ($M_u - M_r$) color. Nevertheless, we concluded that there is a significant subpopulation of radio AGNs that is found in very OD environments at small scales, up to 100 times denser than their control sources. We showed that this component is significant and is not due to any statistical effects of our analysis.

In addition to the above, we have also investigated the probability that there is a link between the radio luminosity of radio AGNs and their environment. Despite a wider radio luminosity range than previous studies, we do not find any

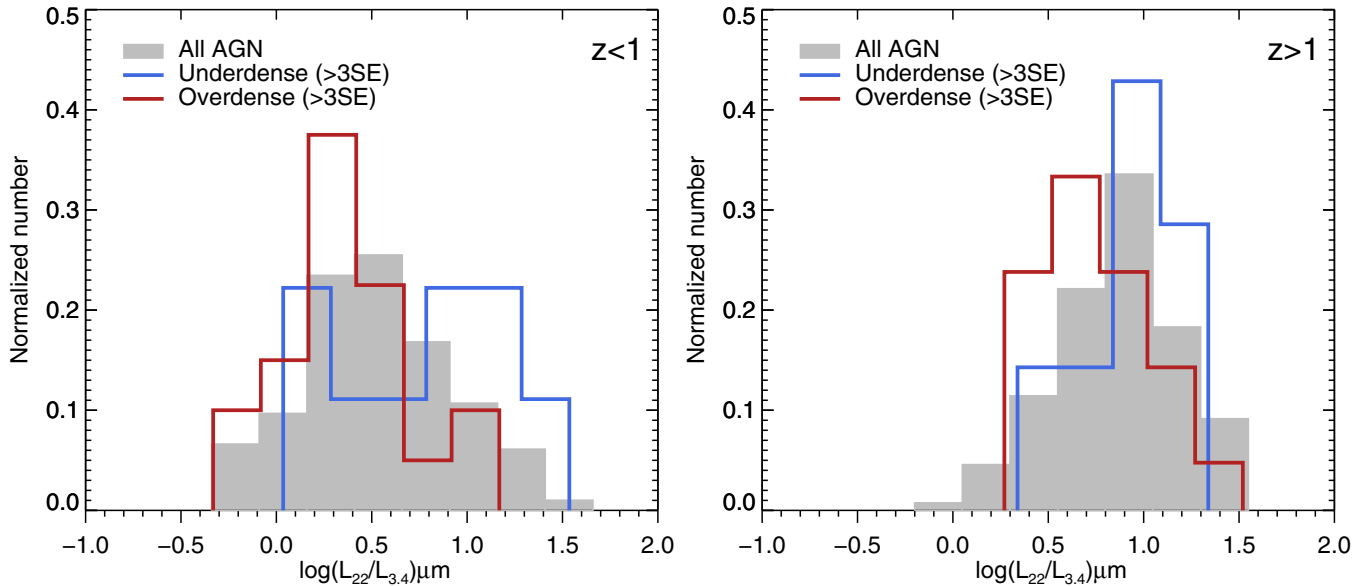


Figure 17. Distribution of the luminosity ratio, in logarithmic scale, between the 22 μm and 3.4 μm bands of *WISE* (*W4* and *W1*, respectively). The distributions of the total radio AGN sample (gray shaded histogram) and the UD and OD subsamples (blue and red open histograms, respectively) are shown. Sources at redshifts < 1 and > 1 are shown separately (left and right panels, respectively).

(A color version of this figure is available in the online journal.)

appreciable trend between more radio-luminous AGNs and more OD environments.

We then turned our attention to the host galaxy properties of the most OD and the most UD radio AGNs in our sample. By looking at the star formation efficiency of these sources and by utilizing our environment results and those of similar studies in the literature, we have put forth a scenario where, in the local universe, a significant component of radio AGNs should be triggered by the feeding of their central supermassive black holes through the mass ejection, in the form of stellar winds, from ongoing star formation in their host galaxies. On the other hand, we expect that the rest of the AGNs should be triggered through accretion of gas from their galactic environment and intercluster medium, albeit with a lower accretion efficiency. This scenario agrees well with previous stipulations about the different origins and phenomenology of low- and high-excitation radio AGNs.

Conversely, the picture seems to change at redshifts above $z \sim 1$. At higher redshifts we do not observe any significant differences between either the sSFR or the accretion efficiency of radio AGNs in the most OD and most UD environments. This leads us to believe that at higher redshifts the availability of cold gas, either in the form of untapped gas reservoirs in galaxies or through galactic interactions and mergers, plays an increasingly important role in the triggering of radio AGNs, independent of their environment.

Follow-up spectroscopic observations of those radio AGNs in the most UD environments can elucidate the true nature and properties of their nuclear activity, in terms of high or low excitation, and can also constrain the star formation in their host galaxies. We plan to pursue a continuation of this study employing a data set with better wavelength coverage in the mid- and far-infrared regime, in order to better constrain the star formation efficiency through detailed modeling of their SEDs. Complimentary integral field spectroscopy observations of nearby radio AGNs in the most UD environments can provide crucial insight about the actual processes fueling these black holes by looking at the density,

velocity, and velocity dispersion of the circumnuclear gas in these galaxies.

We thank the anonymous referee, whose comments have significantly improved this manuscript. This work was supported by the National Research Foundation of Korea (NRF) grant No. 2008-0060544, funded by the Korea government (MSIP). D.K. acknowledges the fellowship support from the grant NRF-2014-Fostering Core Leaders of Future Program, No. 2014-009728, funded by the Korean government. This work is based in part on data obtained as part of the UKIRT Infrared Deep Sky Survey. The United Kingdom Infrared Telescope is operated by the Joint Astronomy Centre on behalf of the Science and Technology Facilities Council of the U.K. This research has made use of NASA’s Astrophysics Data System Bibliographic Services.

APPENDIX A

DEEP VLA SURVEY IN SA22 FIELD

For this work, we use radio observations of the VIMOS-SA22 field with the VLA radio interferometer at 1.4 GHz (Chapman et al. 2004a, 2004b). As these observations and catalogs have not been explicitly presented before, we give here a brief description of the data acquisition, reduction, and source extraction.

The process of obtaining and reducing deep, high-resolution, wide-field 1.4 GHz images is complicated by bandwidth smearing, necessitating the use of spectral-line, pseudo-continuum correlator modes at the National Radio Astronomy Observatory’s¹⁹ (NRAO) VLA, by interference (man-made and solar), and by the presence of dozens of bright (often structurally complex) sources in the primary beam.

For the field under consideration here, SA22, the problems encountered during data reduction were due to the fact that the

¹⁹ NRAO is operated by Associated Universities, Inc., under a cooperative agreement with the National Science Foundation.

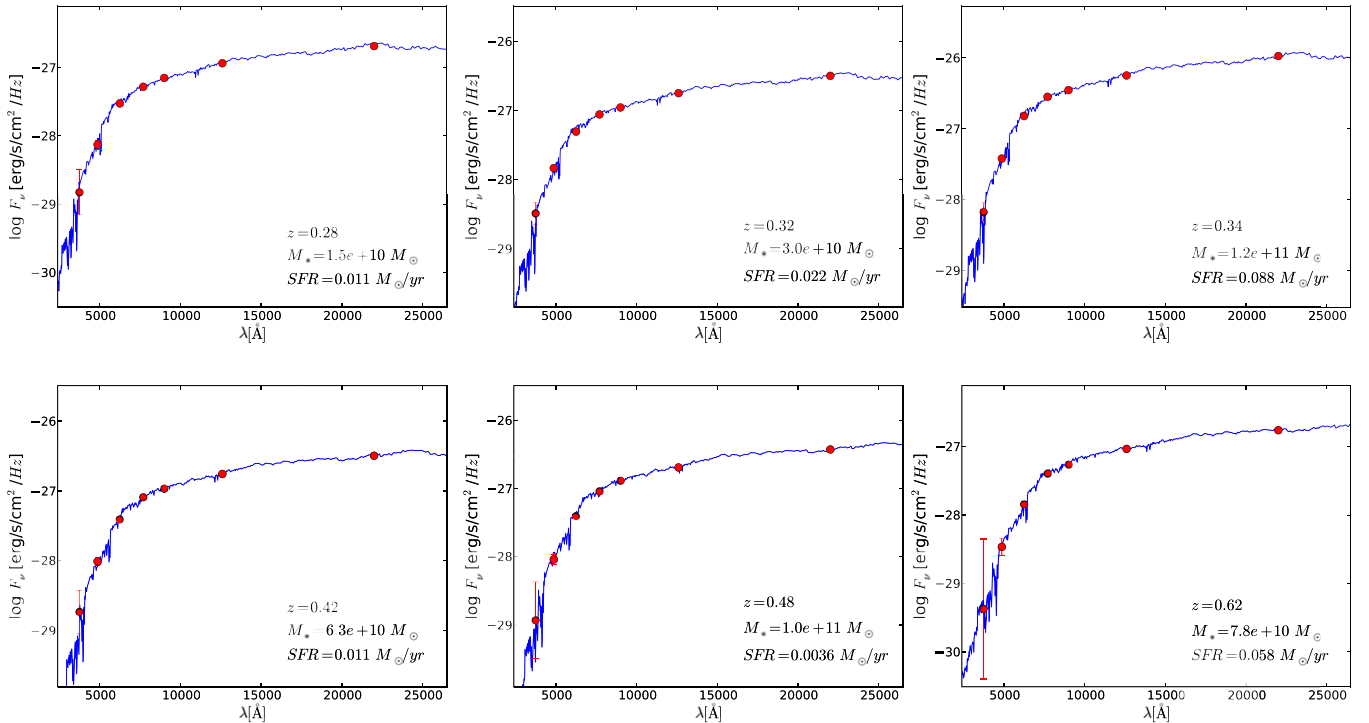


Figure 18. Examples of SED fits using our SED fitting code implementing the stellar population synthesis templates from Bruzual & Charlot (2003) and a delayed SFH (e.g., Lee et al. 2010), and examples of radio AGN sources classified in the OD subsample (see Section 5).

(A color version of this figure is available in the online journal.)

field is crowded with bright sources (the central 100 arcmin² field contains a ~ 200 mJy radio galaxy, as well as several structurally complex FR I/II sources). The field also has relatively poor nearby phase/amplitude calibrators, the best of which is resolved on some baselines. Fortunately, the presence of bright sources allowed self-calibration of the data, correcting the poor initial phase/amplitude calibration.

Data were taken every 5 s in 3.25 MHz channels, 28 in total, centered at 1.4 GHz, recording left-circular and right-circular polarizations. 3C 84 and 3C 286 were used for flux calibration. The phase/amplitude calibrators, 1625+415 and 1035+564, were observed every hour. A total of 45 hr of integration was obtained in A configuration (maximum baseline, 27 km), and 20 hr in B configuration (maximum baseline, 9 km).²⁰

After standard spectral-line calibration and editing of the data and their associated weights, using AIPS, the wide-field imaging task, IMAGR, was used to map the central 10 \times 10 arcmin² field in A config (double the field size for B config). These maps, made with ROBUST = 0 weighting of the visibilities, were used to position CLEAN boxes around the sources, and IMAGR was rerun with 10,000 iterations of the CLEAN algorithm (Högbom 1974; Clark 1980). The CLEAN components thus produced were used as a model for self-calibration (in phase only) using CALIB with a relatively long integration time (~ 1 – 2 minutes) and a low signal-to-noise threshold (3σ – 4σ). Mapping was then repeated, after checks on the CLEAN boxes. The new CLEAN components were subtracted from the visibilities, and the data were clipped to remove spikes and then added back to the CLEAN components. The IMAGR/CALIB loop was then repeated a further four times (though without further clipping), steadily decreasing

the integration time and increasing the signal-to-noise threshold, the final pass of CALIB including both amplitude and phase (with the mean gain modulus of the applied calibration set at unity). This iterative method resulted in the loss of less than 5% of the data. The A and B configuration data were dealt with separately and were not co-added since the complicated noise response was very different in the two configurations. The resulting maps have average noise levels of 8.8 $\mu\text{Jy beam}^{-1}$, with 1".4 resolution, and 22.4 $\mu\text{Jy beam}^{-1}$, with 5".0 resolution.

The area around the brightest objects, which cause the manifestation of sidelobes that could be detected as spurious sources, has been masked, and sources within this area are disregarded for the following. In total, we had to mask three vertical stripe-shaped regions (one for the A configuration map and two for B configuration), losing a total of 16.56 arcsec² and 522 arcsec² for the two configurations, respectively. Owing to the nature of overlap of the two configurations and the location of the masked regions, there are only a handful of sources that are common between the final catalogs of the two configurations. For these cases, we retain the detected sources in the A configuration owing to its superior sensitivity and resolution.

APPENDIX B

SED FITTING

In this section, we give examples of the best SED fits derived for the radio sources classified as radio AGNs owing to their luminosity. In Figure 18 we show examples for radio AGNs in the OD subsample, while Figure 19 shows examples for radio AGNs in the UD subsample. Redshifts and derived stellar masses and SFRs are given for each individual source. The SEDs are shown in the observed wavelength.

²⁰ Dates of observations were “2003-07-06” and “1998-10-03” for A and B configurations, respectively.

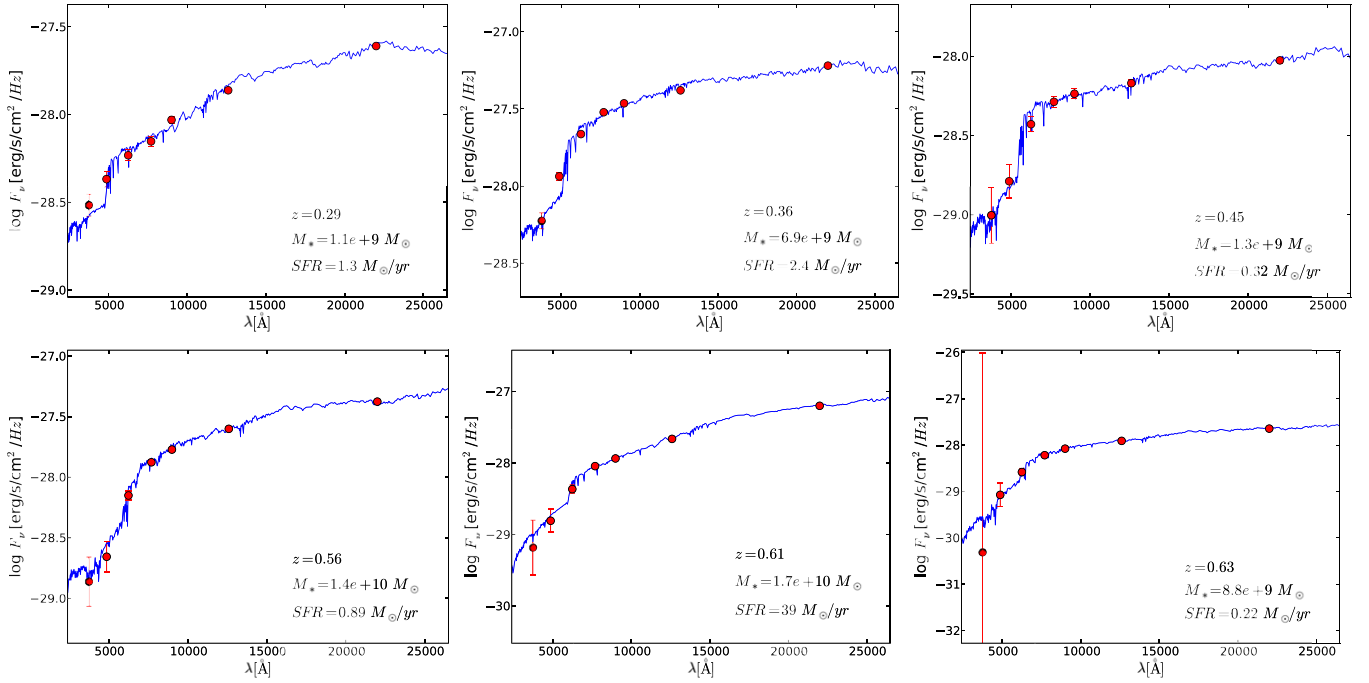


Figure 19. As in Figure 18, but here we show examples of radio AGN sources classified in the UD subsample (see Section 5).
(A color version of this figure is available in the online journal.)

REFERENCES

- Aird, J., Nandra, K., Laird, E. S., et al. 2010, *MNRAS*, 401, 2531
- Alberts, S., Pope, A., Brodwin, M., et al. 2014, *MNRAS*, 437, 437
- Arnouts, S., Cristiani, S., Moscardini, L., et al. 1999, *MNRAS*, 310, 540
- Becker, R. H., White, R. L., & Helfand, D. J. 1995, *ApJ*, 450, 559
- Bennert, N., Canalizo, G., Jungwiert, B., et al. 2008, *ApJ*, 677, 846
- Bertin, E., & Arnouts, S. 1996, *A&AS*, 117, 393
- Bertin, E., Mellier, Y., Radovich, M., et al. 2002, in ASP Conf. Ser. 281, *Astronomical Data Analysis Software and Systems XI*, ed. D. A. Bohlender, D. Durand, & T. H. Handley (San Francisco, CA: ASP), 228
- Best, P. N. 2004, *MNRAS*, 351, 70
- Best, P. N., & Heckman, T. M. 2012, *MNRAS*, 421, 1569
- Best, P. N., Kauffmann, G., Heckman, T. M., et al. 2005a, *MNRAS*, 362, 25
- Best, P. N., Kauffmann, G., Heckman, T. M., & Ivezić, Ž. 2005b, *MNRAS*, 362, 9
- Blanton, M. R., & Moustakas, J. 2009, *ARA&A*, 47, 159
- Bradshaw, E. J., Almaini, O., Hartley, W. G., et al. 2011, *MNRAS*, 415, 2626
- Bruzual, G., & Charlot, S. 2003, *MNRAS*, 344, 1000
- Calzetti, D., Armus, L., Bohlin, R. C., et al. 2000, *ApJ*, 533, 682
- Canalizo, G., Bennert, N., Jungwiert, B., et al. 2007, *ApJ*, 669, 801
- Canalizo, G., & Stockton, A. 2001, *ApJ*, 555, 719
- Casali, M., Adamson, A., Alves de Oliveira, C., et al. 2007, *A&A*, 467, 777
- Chabrier, G. 2003, *PASP*, 115, 763
- Chapman, S. C., Scott, D., Windhorst, R. A., et al. 2004a, *ApJ*, 606, 85
- Chapman, S. C., Smail, I., Windhorst, R., Muxlow, T., & Ivison, R. J. 2004b, *ApJ*, 611, 732
- Cisternas, M., Jahnke, K., Inskip, K. J., et al. 2011, *ApJ*, 726, 57
- Clark, B. G. 1980, *A&A*, 89, 377
- Coil, A. L., Newman, J. A., Croton, D., et al. 2008, *ApJ*, 672, 153
- Condon, J. J. 1992, *ARA&A*, 30, 575
- Condon, J. J., Cotton, W. D., Greisen, E. W., et al. 1998, *AJ*, 115, 1693
- Cooper, M. C., Newman, J. A., Madgwick, D. S., et al. 2005, *ApJ*, 634, 833
- Davies, R. I., Müller Sánchez, F., Genzel, R., et al. 2007, *ApJ*, 671, 1388
- Dicken, D., Tadhunter, C., Axon, D., et al. 2012, *ApJ*, 745, 172
- Donoso, E., Li, C., Kauffmann, G., Best, P. N., & Heckman, T. M. 2010, *MNRAS*, 407, 1078
- Downes, A. J. B., Peacock, J. A., Savage, A., & Carrie, D. R. 1986, *MNRAS*, 218, 31
- Dressler, A. 1980, *ApJ*, 236, 351
- Elbaz, D., Dickinson, M., Hwang, H. S., et al. 2011, *A&A*, 533, A119
- Ellison, S. L., Patton, D. R., Mendel, J. T., & Scudder, J. M. 2011, *MNRAS*, 418, 2043
- Fabian, A. C. 1994, *ARA&A*, 32, 277
- Fanaroff, B. L., & Riley, J. M. 1974, *MNRAS*, 167, 31
- Fanidakis, N., Baugh, C. M., Benson, A. J., et al. 2011, *MNRAS*, 410, 53
- Gürkan, G., Hardcastle, M. J., & Jarvis, M. J. 2014, *MNRAS*, 438, 1149
- Hardcastle, M. J., Ching, J. H. Y., Virdee, J. S., et al. 2013, *MNRAS*, 429, 2407
- Hardcastle, M. J., Evans, D. A., & Croston, J. H. 2007, *MNRAS*, 376, 1849
- Heckman, T. M., Smith, E. P., Baum, S. A., et al. 1986, *ApJ*, 311, 526
- Herbert, P. D., Jarvis, M. J., Willott, C. J., et al. 2010, *MNRAS*, 406, 1841
- Hernquist, L. 1989, *Natur*, 340, 687
- Hodge, J. A., Karim, A., Smail, I., et al. 2013, *ApJ*, 768, 91
- Högbom, J. A. 1974, *A&AS*, 15, 417
- Hopkins, A. M., & Beacom, J. F. 2006, *ApJ*, 651, 142
- Hopkins, P. F., Cox, T. J., Kereš, D., & Hernquist, L. 2008, *ApJS*, 175, 390
- Hopkins, P. F., & Hernquist, L. 2006, *ApJS*, 166, 1
- Hopkins, P. F., Hernquist, L., Cox, T. J., et al. 2006, *ApJS*, 163, 1
- Ilbert, O., Arnouts, S., McCracken, H. J., et al. 2006, *A&A*, 457, 841
- Ilbert, O., Tresse, L., Zucca, E., et al. 2005, *A&A*, 439, 863
- Im, M., Ko, J., Cho, Y., et al. 2010, *JKAS*, 43, 75
- Ivezić, Ž., Menou, K., Knapp, G. R., et al. 2002, *AJ*, 124, 2364
- Ivison, R. J., Greve, T. R., Dunlop, J. S., et al. 2007, *MNRAS*, 380, 199
- Jarvis, M. J., Bonfield, D. G., Bruce, V. A., et al. 2013, *MNRAS*, 428, 1281
- Kalfountzou, E., Stevens, J. A., Jarvis, M. J., et al. 2014, *MNRAS*, 442, 1181
- Karouzos, M., Britzen, S., Eckart, A., Witzel, A., & Zensus, A. 2010, *A&A*, 519, A62
- Karouzos, M., Im, M., Trichas, M., et al. 2014a, *ApJ*, 784, 137
- Karouzos, M., Jarvis, M. J., & Bonfield, D. 2014b, *MNRAS*, 439, 861
- Kauffmann, G., & Haehnelt, M. 2000, *MNRAS*, 311, 576
- Kauffmann, G., Heckman, T. M., Tremonti, C., et al. 2003a, *MNRAS*, 346, 1055
- Kauffmann, G., Heckman, T. M., White, S. D. M., et al. 2003b, *MNRAS*, 341, 33
- Kauffmann, G., White, S. D. M., Heckman, T. M., et al. 2004, *MNRAS*, 353, 713
- Kellermann, K. I., Sramek, R., Schmidt, M., Shaffer, D. B., & Green, R. 1989, *AJ*, 98, 1195
- Kereš, D., Katz, N., Weinberg, D. H., & Davé, R. 2005, *MNRAS*, 363, 2
- Kim, J.-W., Edge, A. C., Wake, D. A., & Stott, J. P. 2011, *MNRAS*, 410, 241
- Kistler, M. D., Yuksel, H., & Hopkins, A. M. 2013, arXiv:1305.1630
- Kocevski, D. D., Faber, S. M., Mozena, M., et al. 2012, *ApJ*, 744, 148
- Komatsu, E., Smith, K. M., Dunkley, J., et al. 2011, *ApJS*, 192, 18
- Lawrence, A., Warren, S. J., Almaini, O., et al. 2007, *MNRAS*, 379, 1599
- Le Fèvre, O., Vettolani, G., Garilli, B., et al. 2005, *A&A*, 439, 845
- Lee, S.-K., Ferguson, H. C., Somerville, R. S., et al. 2014, *ApJ*, 783, 81
- Lee, S.-K., Ferguson, H. C., Somerville, R. S., Wiklind, T., & Gialalisco, M. 2010, *ApJ*, 725, 1644

- Lee, S.-K., Idzi, R., Ferguson, H. C., et al. 2009, *ApJS*, **184**, 100
- Lietzen, H., Heinämäki, P., Nurmi, P., et al. 2011, *A&A*, **535**, A21
- Lotz, J. M., Jonsson, P., Cox, T. J., et al. 2011, *ApJ*, **742**, 103
- Lotz, J. M., Jonsson, P., Cox, T. J., & Primack, J. R. 2008, *MNRAS*, **391**, 1137
- Madau, P. 1995, *ApJ*, **441**, 18
- Mateos, S., Alonso-Herrero, A., Carrera, F. J., et al. 2012, *MNRAS*, **426**, 3271
- Mauch, T., & Sadler, E. M. 2007, *MNRAS*, **375**, 931
- Miller, C. J., Nichol, R. C., Gómez, P. L., Hopkins, A. M., & Bernardi, M. 2003, *ApJ*, **597**, 142
- Navarro, J. F., Frenk, C. S., & White, S. D. M. 1996, *ApJ*, **462**, 563
- Navarro, J. F., Frenk, C. S., & White, S. D. M. 1997, *ApJ*, **490**, 493
- Norman, C., & Scoville, N. 1988, *ApJ*, **332**, 124
- Pace, C., & Salim, S. 2014, *ApJ*, **785**, 66
- Padovani, P., Mainieri, V., Tozzi, P., et al. 2009, *ApJ*, **694**, 235
- Park, W.-K., Pak, S., Im, M., et al. 2012, *PASP*, **124**, 839
- Peng, Y.-j., Lilly, S. J., Kovač, K., et al. 2010, *ApJ*, **721**, 193
- Pierce, C. M., Lotz, J. M., Primack, J. R., et al. 2010, *MNRAS*, **405**, 718
- Polletta, M., Tajer, M., Maraschi, L., et al. 2007, *ApJ*, **663**, 81
- Ramos Almeida, C., Bessiere, P. S., Tadhunter, C. N., et al. 2013, *MNRAS*, **436**, 997
- Ramos Almeida, C., Tadhunter, C. N., Inskip, K. J., et al. 2011, *MNRAS*, **410**, 1550
- Richards, G. T., Strauss, M. A., Fan, X., et al. 2006, *AJ*, **131**, 2766
- Rodighiero, G., Cimatti, A., Gruppioni, C., et al. 2010, *A&A*, **518**, L25
- Salvato, M., Ilbert, O., Hasinger, G., et al. 2011, *ApJ*, **742**, 61
- Sanders, D. B., Soifer, B. T., Elias, J. H., Neugebauer, G., & Matthews, K. 1988, *ApJL*, **328**, L35
- Satyapal, S., Ellison, S. L., McAlpine, W., et al. 2014, *MNRAS*, **441**, 1297
- Scoville, N., Arnouts, S., Aussel, H., et al. 2013, *ApJS*, **206**, 3
- Serber, W., Bahcall, N., Ménard, B., & Richards, G. 2006, *ApJ*, **643**, 68
- Seymour, N., Dwelly, T., Moss, D., et al. 2008, *MNRAS*, **386**, 1695
- Shapley, A. E., Steidel, C. C., Erb, D. K., et al. 2005, *ApJ*, **626**, 698
- Shen, Y., Richards, G. T., Strauss, M. A., et al. 2011, *ApJS*, **194**, 45
- Skibba, R. A., Smith, M. S. M., Coil, A. L., et al. 2014, *ApJ*, **784**, 128
- Strateva, I., Ivezić, Ž., Knapp, G. R., et al. 2001, *AJ*, **122**, 1861
- Tasse, C., Best, P. N., Röttgering, H., & Le Borgne, D. 2008, *A&A*, **490**, 893
- Tasse, C., Röttgering, H., & Best, P. N. 2011, *A&A*, **525**, A127
- Urry, C. M., & Padovani, P. 1995, *PASP*, **107**, 803
- van Velzen, S., Falcke, H., Schellart, P., Nierstenhöfer, N., & Kampert, K.-H. 2012, *A&A*, **544**, A18
- Villforth, C., Hamann, F., Rosario, D. J., et al. 2014, *MNRAS*, **439**, 3342
- White, R. L., Becker, R. H., Helfand, D. J., & Gregg, M. D. 1997, *ApJ*, **475**, 479
- Wiklund, T., Conelice, C. J., Dahlen, T., et al. 2014, *ApJ*, **785**, 111
- Wild, V., Heckman, T., & Charlot, S. 2010, *MNRAS*, **405**, 933
- Wild, V., Kauffmann, G., Heckman, T., et al. 2007, *MNRAS*, **381**, 543
- Winters, J. M., Le Bertre, T., Jeong, K. S., Nyman, L.-Å., & Epchtein, N. 2003, *A&A*, **409**, 715
- Worpel, H., Brown, M. J. I., Jones, D. H., Floyd, D. J. E., & Beutler, F. 2013, *ApJ*, **772**, 64
- Wright, E. L., Eisenhardt, P. R. M., Mainzer, A. K., et al. 2010, *AJ*, **140**, 1868
- Zehavi, I., Zheng, Z., Weinberg, D. H., et al. 2011, *ApJ*, **736**, 59